



# Global atmospheric inversion of the anthropogenic $\text{NH}_3$ emissions over 2019–2022 using the LMDZ-INCA chemistry transport model and the IASI $\text{NH}_3$ observations

Pramod Kumar<sup>1</sup>, Grégoire Broquet<sup>1</sup>, Didier Hauglustaine<sup>1</sup>, Maureen Beaudor<sup>1,a</sup>, Lieven Clarisse<sup>2</sup>, Martin Van Damme<sup>2,3</sup>, Pierre Coheur<sup>2</sup>, Anne Cozic<sup>1</sup>, Bo Zheng<sup>4</sup>, Beatriz Revilla Romero<sup>5</sup>, Antony Delavois<sup>6</sup>, and Philippe Ciais<sup>1</sup>

<sup>1</sup>Laboratoire des Sciences du Climat et de l'Environnement (LSCE/IPSL), CEA-CNRS-UVSQ, Université Paris-Saclay, Gif-sur-Yvette, France

<sup>2</sup>Spectroscopy, Quantum Chemistry and Atmospheric Remote Sensing, Université libre de Bruxelles (ULB), Brussels, Belgium

<sup>3</sup>Royal Belgian Institute for Space Aeronomy, Brussels, Belgium

<sup>4</sup>Institute of Environment and Ecology, Tsinghua Shenzhen International Graduate School, Tsinghua University, Shenzhen, China

<sup>5</sup>GMV, Remote Sensing & Geospatial Analytics Division, Madrid, Spain

<sup>6</sup>European Space Agency, ESRIN, Via Galileo Galilei, Frascati, Italy

<sup>a</sup>currently at: High Meadows Environmental Institute, Princeton University, Princeton, NJ 08540, USA

**Correspondence:** Pramod Kumar (pramod.kumar@lsce.ipsl.fr)

Received: 14 January 2025 – Discussion started: 17 February 2025

Revised: 15 July 2025 – Accepted: 16 July 2025 – Published: 8 October 2025

**Abstract.** Ammonia ( $\text{NH}_3$ ) emissions have been on a continuous rise due to extensive fertilizer usage in agriculture and increasing production of manure and livestock. However, the current global-to-national  $\text{NH}_3$  emission inventories exhibit large uncertainties. We provide atmospheric inversion estimates of the global  $\text{NH}_3$  emissions over 2019–2022 at  $1.27^\circ \times 2.5^\circ$  horizontal and daily (at 10 d scale) resolution. We use IASI-ANNI-NH3-v4 satellite observations, simulations of  $\text{NH}_3$  concentrations with the chemistry transport model LMDZ-INCA, and the finite difference mass-balance approach for inversions of global  $\text{NH}_3$  emissions. We take advantage of the averaging kernels provided in the IASI-ANNI-NH3-v4 dataset by applying them consistently to the LMDZ-INCA  $\text{NH}_3$  simulations for comparison to the observations and then to invert emissions. The average global anthropogenic  $\text{NH}_3$  emissions over 2019–2022 are estimated as  $\sim 97$  ( $94$ – $100$ )  $\text{Tg yr}^{-1}$ , which is  $\sim 61\%$  ( $\sim 55\%$ – $65\%$ ) higher than the prior Community Emissions Data System (CEDS) inventory's anthropogenic  $\text{NH}_3$  emissions and significantly higher than two other global inventories: CAMS's anthropogenic  $\text{NH}_3$  emissions (by a factor of  $\sim 1.8$ ) and the Calculation of AMmonia Emissions in ORCHIDEE (CAMEO) agricultural and natural soil  $\text{NH}_3$  emissions (by  $\sim 1.4$  times). The global and regional budgets are mostly within the range of other inversion estimates. The analysis provides confidence in their seasonal variability and continental- to regional-scale budgets. Our analysis shows a rise in  $\text{NH}_3$  emissions by  $\sim 5\%$  to  $\sim 37\%$  during the COVID-19 lockdowns in 2020 over different regions compared to the same-period emissions in 2019. However, this rise is probably due to a decrease in atmospheric  $\text{NH}_3$  sinks due to the decline in  $\text{NO}_x$  and  $\text{SO}_2$  emissions during the lockdowns.

## 1 Introduction

Ammonia (NH<sub>3</sub>) plays a critical role in both atmospheric chemistry and the ecosystem's nitrogen and carbon cycling, with significant implications for air quality and human health, climate change, and agriculture. Ammonia in the Earth's atmosphere originates from both natural and anthropogenic sources, with the latter dominating emissions from the former. The agricultural sector is the largest source of NH<sub>3</sub> emissions, contributing more than 81 % of the total global NH<sub>3</sub> emissions (Van Damme et al., 2021; Wyer et al., 2022), and other anthropogenic sources of NH<sub>3</sub> mainly stem from domestic, vehicular, waste water treatment, and industrial activities (Behera et al., 2013a; Sutton et al., 2013). Global future NH<sub>3</sub> emissions in 2100 are projected to increase by 30 % to 50 % compared to present-day levels, depending on the different Shared Socioeconomic Pathways scenarios (Beaudor et al., 2025). Precise information on the NH<sub>3</sub> sources and quantitative attribution of emissions to these sources and atmospheric NH<sub>3</sub> concentration observations are essential in evaluating the impacts of NH<sub>3</sub> on ecosystems, climate, air quality, and human health and in formulating effective mitigation measures (Zhu et al., 2015). Timely estimates of global anthropogenic NH<sub>3</sub> emissions are needed to formulate effective control strategies to reduce such emissions activities (Behera et al., 2013).

Bottom-up NH<sub>3</sub> emission inventories provide data on NH<sub>3</sub> sources and their emissions (Beaudor et al., 2023; Bouwman et al., 1997; Vira et al., 2020), enabling their integration into atmospheric chemistry transport and climate models to simulate atmospheric ammonia concentrations and making it possible to assess the impacts of NH<sub>3</sub> emissions. However, significant uncertainties are inherent in bottom-up NH<sub>3</sub> emission inventories across spatiotemporal scales (Behera et al., 2013; Luo et al., 2022; Sutton et al., 2013), stemming from the constraints of limited NH<sub>3</sub> emission activity data and emission factors, high uncertainty of agriculture statistics, and a lack of recent information (Chen et al., 2021; Crippa et al., 2018; Xu et al., 2019). In situ measurements are essential for accurately developing NH<sub>3</sub> emission inventories and for the inversion of NH<sub>3</sub> emissions, as well as for evaluating these emissions. However, the scarcity of in situ NH<sub>3</sub> measurements worldwide contributed to significant uncertainties in NH<sub>3</sub> emissions and in our understanding of NH<sub>3</sub> sources and their distributions (Zhu et al., 2015). Advancements in satellite measurements of columnar NH<sub>3</sub> abundance in the atmosphere in the past decades provide high-spatiotemporal-resolution column concentration data, and inversion methods are progressively enhancing our ability to derive NH<sub>3</sub> emissions. For the atmospheric inverse modeling of the NH<sub>3</sub> emissions, satellite observations offer valuable data density and coverage, thus mitigating some of the limitations of the use of in situ NH<sub>3</sub> measurements, enabling a more comprehensive assessment of NH<sub>3</sub> emissions. The recent NH<sub>3</sub> emission estimates based on satellite observations exhibit signifi-

cant differences at both regional and global scales when compared to those reported by the bottom-up inventories (Cao et al., 2020; Chen et al., 2021; Van Damme et al., 2018; Luo et al., 2022; Evangeliou et al., 2021; Dammers et al., 2022). However, the satellite data also have some limitations, often lacking clear signals from the emissions outside the strongly polluted regions, bearing potential errors due to interference from other atmospheric constituents and the complexity of their validation and calibration, and being sensitive to cloud cover, providing incomplete coverage in certain regions in the presence of clouds.

Currently, satellite NH<sub>3</sub> observations are available from instruments such as the Atmospheric Infrared Sounder (AIRS) on the NASA EOS Aqua satellite (Warner et al., 2016), the Aura Tropospheric Emission Spectrometer (TES) on board the EOS Aura satellite (Beer et al., 2008), three of the Infrared Atmospheric Sounding Interferometer (IASI) series of instruments on the MetOp (Meteorological Operational satellite program) satellites (Clarisse et al., 2009; Van Damme et al., 2021), the Thermal And Near-infrared Spectrometer for Observation–Fourier Transform Spectrometer (TANSO-FTS) on board the Greenhouse Gases Observing Satellite (GOSAT) (Someya et al., 2020), and the three Cross-track Infrared Sounder (CrIS) instruments on board the Suomi National Polar-orbiting Partnership (Suomi-NPP) satellites (Shephard et al., 2020). These datasets vary in their data record lengths, spatial coverage, and retrieval approaches. The NH<sub>3</sub> observations derived from the IASI and CrIS measurements, which have similar instrumental characteristics but employ different retrieval approaches, are the most commonly used satellite data for constraining NH<sub>3</sub> emission estimates. The IASI NH<sub>3</sub> product is a widely used dataset, as it provides continuous, long-term sampling commencing from 2007, with twice-daily coverage across the globe. Except for its first version, subsequent versions of the IASI NH<sub>3</sub> data products are based on the Artificial Neural Network for IASI (ANNI) approach for the retrieval of NH<sub>3</sub> total columns (Van Damme et al., 2017, 2021; Whitburn et al., 2016). However, the absence of the vertical averaging kernel (AK) in the IASI ANNI NH<sub>3</sub> previous products hindered their utility for comprehensive comparisons to the atmospheric chemistry transport model and its suitability for assimilation in atmospheric inversion processes for NH<sub>3</sub> emission estimations. The AK is proportional to the measurement vertical sensitivity profile and also describes the vertical structure of the impact of a priori information on the retrieval of NH<sub>3</sub> columns. When comparing a chemistry transport model against the satellite column retrievals, e.g., in satellite data assimilation processes, the application of the AK should remove the influence of errors resulting from the a priori (or an assumed) atmospheric NH<sub>3</sub> vertical profile used in the retrievals in the model–satellite comparison (Eskes and Boersma, 2003). Using synthetic satellite column observations of another short-lived species (NO<sub>2</sub>), Cooper et al. (2020) examined the impact of differences between the

modeled and a priori atmospheric vertical  $\text{NO}_2$  profiles on the inversion of  $\text{NO}_x$  emission estimates and found that discrepancies led to an up to 30 % increase in root mean square errors for realistic conditions over polluted regions, with inverted emission errors rising as the difference between simulated and a priori profiles increases. The application of AK enables the model-retrieval comparison to be independent of the a priori profile (Cooper et al., 2020; Douros et al., 2023). Recently, Clarisse et al. (2023) presented a new version 4 of the ANNI retrieval framework including, for the first time, vertical AK in the IASI  $\text{NH}_3$  data product. In this study, we use this new version 4 of the IASI ANNI  $\text{NH}_3$  dataset for comparison to the global chemistry transport model simulations and for the atmospheric inversion of the global  $\text{NH}_3$  emissions.

In recent years, numerous studies have used satellite observations, mostly IASI and CrIS, to estimate  $\text{NH}_3$  emissions over specific regions (Cao et al., 2020, 2022; Chen et al., 2021; Ding et al., 2024; Fortems-Cheiney et al., 2020; Tichý et al., 2023; Xia et al., 2025) or across the globe (Dammers et al., 2022; Evangeliou et al., 2021; Luo et al., 2022). Some recent regional-scale inversion studies over the USA (Cao et al., 2020; Chen et al., 2021), China (Jin et al., 2023; Momeni et al., 2024), UK (Marais et al., 2021), and Europe (Cao et al., 2022; Ding et al., 2024; van der Graaf et al., 2022) show approximately 20 %–100 % differences between the inversion-based and the bottom-up  $\text{NH}_3$  emissions. The  $\text{NH}_3$  inversion problem raises challenges and requires a high spatial resolution of the emissions because the  $\text{NH}_3$  emissions are highly localized due to the short lifetime of a few hours to a day of ammonia in the atmosphere. The impact of the atmospheric chemistry challenges the linearization underlying the traditional inversion approaches or the use of relatively simple models of the atmospheric chemistry and transport. The conventional variational or Kalman filter approaches, which are among the most sophisticated ones, have been used for regional-scale inversions (Cao et al., 2020, 2022; Ding et al., 2024; Jin et al., 2023). However, covering the globe at a suitable spatial resolution represents an inversion problem whose dimensions make the application of such approaches very demanding in terms of computational cost. That is probably why, compared to regional studies, global inversions of  $\text{NH}_3$  emissions based on satellite observations are relatively scarce (Van Damme et al., 2018; Dammers et al., 2022; Evangeliou et al., 2021; Luo et al., 2022). Studies such as Van Damme et al. (2018) and Dammers et al. (2019) covered emissions worldwide but focused on the detection and estimation of  $\text{NH}_3$  large point sources or hotspot areas. Using high-resolution maps of atmospheric ammonia from IASI, Van Damme et al. (2018) detected 248  $\text{NH}_3$  hotspot locations and large source regions across the globe and reported that the satellite-data-constrained  $\text{NH}_3$  emissions for the source regions vary within a factor of 3 from the corresponding estimates extracted from the Emissions Database for Global Atmospheric Research (EDGAR) emission inven-

tory. However, the emissions from these detected large  $\text{NH}_3$  point sources or source regions account for only a small fraction of the overall global  $\text{NH}_3$  emissions budget (Dammers et al., 2019). For instance, the cumulative  $\text{NH}_3$  emissions from the 249 point sources identified by Dammers et al. (2019) contributed to merely 5 % of the total global  $\text{NH}_3$  emissions in the Hemispheric Transport Atmospheric Pollution version 2 (HTAPv2) inventory.

Only very few global-scale inversion studies provided more comprehensive time series of full  $\text{NH}_3$  emission maps using computationally intensive inversion frameworks. Recently, Dammers et al. (2022) derived global  $\text{NH}_3$  emission maps at a high spatial resolution ( $0.2^\circ \times 0.2^\circ$ ) based on a multi-source Gaussian plume method using CrIS observations, discarding any chemistry or aerosol mechanism associated with the short-lived species  $\text{NH}_3$  in the multi-source Gaussian plume method. They showed that satellite-based total  $\text{NH}_3$  emissions over the globe are  $\sim 1.8$  times higher than those reported in previously identified anthropogenic  $\text{NH}_3$  source locations in the CAMS-GLOB-ANT v4.2 global anthropogenic  $\text{NH}_3$  emission inventory, and the total estimates rise to  $\sim 4$  times greater when newly detected anthropogenic and natural sources are taken into account. However, this approach also introduces uncertainties in the estimates due to the assumption of a globally constant atmospheric lifetime for  $\text{NH}_3$ , which is a limiting factor because chemical loss and deposition are highly variable processes that can change the lifetime drastically (Van Damme et al., 2018), and uncertainties in plume spread, wind speed, and wind direction when fitting a multi-source Gaussian plume model to the observations.

In two recent studies of the global inversion of  $\text{NH}_3$  emissions using previous versions of the IASI ANNI  $\text{NH}_3$  data products, Evangeliou et al. (2021) and Luo et al. (2022) estimated long-term monthly global  $\text{NH}_3$  emissions over a decade starting from 2008 and reported their estimates to be higher than those in the bottom-up inventories. However, significance differences were observed between these two  $\text{NH}_3$  emission estimates. In both studies, inversions rely on the  $\text{NH}_3$  lifetime, diagnosed differently from the simulations of different global chemistry transport models (CTMs), and the modeled  $\text{NH}_3$  total columns. Evangeliou et al. (2021) applied a basic mass-balance inversion approach to estimate monthly  $\text{NH}_3$  emissions in each grid cell as a ratio of the observed total  $\text{NH}_3$  column from IASI and the lifetime of  $\text{NH}_3$  computed from CTM simulations. Using a previous version of IASI  $\text{NH}_3$  observations, Luo et al. (2022) modified the basic mass-balance approach used in Evangeliou et al. (2021) by updating the prior  $\text{NH}_3$  emissions with an additive correction term. This correction is proportional to the difference between the observed and modeled  $\text{NH}_3$  columns and inversely proportional to the  $\text{NH}_3$  lifetime estimated by accounting for the deposition fluxes of the whole  $\text{NH}_x$  ( $\text{NH}_3 + \text{NH}_4^+$ ) family instead of using only the  $\text{NH}_3$  losses. However, estimating the lifetime of  $\text{NH}_3$  in the atmosphere is more complex due

to the impact of transport mechanisms, loss of atmospheric NH<sub>3</sub> by the formation of ammonium sulfate or ammonium nitrate particles (Cao et al., 2020), and non-linearities in NH<sub>3</sub>-related chemistry affecting deposition and concentration. Changes in NH<sub>3</sub> concentrations due to emission affect its lifetime through its interaction with other trace chemical species like SO<sub>2</sub>, NO<sub>x</sub>, HCl, and HONO (Behera et al., 2013), and the basic mass-balance approaches in Evangeliou et al. (2021) and Luo et al. (2022) do not consider the impact of NH<sub>3</sub> emission changes in their estimation of NH<sub>3</sub> lifetime in atmospheric inversions, which may affect the accuracy of emission estimates.

Variations of the mass-balance inversion methodology, such as the finite difference mass-balance (FDMB) approach (Cooper et al., 2017; Lamsal et al., 2011), have been proposed for atmospheric inversion of emissions of short-lived species, which aims to reduce errors in basic mass-balance methods due to non-linear sensitivity between species emissions and ambient concentrations. The FDMB inversion approach is computationally efficient for the global-scale inversions at coarse resolutions, and it has been widely used for estimating anthropogenic surface emissions of short-lived species like NO<sub>x</sub> and SO<sub>2</sub> at global and regional scales (Cooper et al., 2017; Lamsal et al., 2011). It derives the fluxes by scaling a priori emission estimates, usually derived from bottom-up inventories. This scaling is derived from the computation of the local sensitivity of concentrations to local emission changes from simulations with a CTM and from the relative differences between observations and the modeled columns. Only a few studies have investigated the FDMB approach for NH<sub>3</sub> emission inversion at regional scales: Momeni et al. (2024) and Li et al. (2019). They applied the iterative FDMB approach to constrain the NH<sub>3</sub> emissions of East Asia with CrIS and North America with IASI satellite observations. In this study, we investigate the use of the FDMB approach at the global scale to derive maps of the NH<sub>3</sub> emissions at a relatively high temporal resolution worldwide. While earlier global-scale inversion studies by Luo et al. (2022) and Evangeliou et al. (2021) derived NH<sub>3</sub> emission estimates at the 1-month scale, we aim to provide daily estimates at the 10 d scale (deriving 10 d running average). The FDMB inversion approach involves a chemistry transport model for simulations of NH<sub>3</sub> concentrations. We use the global chemistry–aerosols transport model LMDZ-INCA (Hauglustaine et al., 2004, 2014) for global NH<sub>3</sub> concentration simulations. Our LMDZ-INCA model configuration has a relatively high spatial resolution of 1.27° × 2.5° (latitude × longitude) horizontally and 79 vertical levels. The absence of the averaging kernel in previous versions of the IASI ANNI NH<sub>3</sub> data products used in the previous inversion studies prevented utilization of this information to integrate the modeled NH<sub>3</sub> profile consistently with the IASI NH<sub>3</sub> retrievals. This limitation may have impacted the final NH<sub>3</sub> emission estimates. In this study, we take advantage of the availability of AKs in version 4 of the IASI NH<sub>3</sub> product

for suitable assimilation of such data into a global inversion framework relying on a CTM. The application of AK in our global atmospheric inversion of NH<sub>3</sub> emissions with the new version 4 of the IASI NH<sub>3</sub> retrievals is one of the main features in this study.

Here, we estimate global daily (as a 10 d running average) anthropogenic NH<sub>3</sub> emissions over the land at 1.27° × 2.5° horizontal resolution across a period of 4 years from 2019 to 2022 using the new version 4 of the IASI ANNI NH<sub>3</sub> data product and the FDMB inversion approach (Cooper et al., 2017; Lamsal et al., 2011). We first compare the LMDZ-INCA model global NH<sub>3</sub> simulations against the IASI NH<sub>3</sub> observations to assess our model's performance and its suitability for global inversions of NH<sub>3</sub> emissions. In both model–satellite comparisons and inversions, we take advantage of averaging kernels provided in version 4 of the IASI ANNI NH<sub>3</sub> data product to remove the impact of the vertical NH<sub>3</sub> profile assumption in the retrievals. We present and discuss the results of our model comparison analysis with the IASI NH<sub>3</sub> observations and the global inversions of the NH<sub>3</sub> emissions at both global and regional scales, considering temporal scales ranging from daily (10 d scale) to monthly, seasonal, and annual. We evaluate our inversion approach and emissions estimates by conducting LMDZ-INCA simulations using the optimized NH<sub>3</sub> emissions and comparing the model results with the IASI NH<sub>3</sub> observations. Finally, we compare our estimated global NH<sub>3</sub> emissions with independent global bottom-up inventories and other estimated NH<sub>3</sub> emissions over the globe and over the selected regions. The structure of the paper is as follows. Section 2 describes the new version 4 of the IASI NH<sub>3</sub> observations, the chemistry transport model and its setup for global NH<sub>3</sub> concentration simulations, our strategy to compare model NH<sub>3</sub> simulations with the satellite observations, and the FDMB inversion approach used for global daily NH<sub>3</sub> emission estimations. Section 3 presents the results, followed by a discussion of those results and the limitations of the study in Sect. 4. Key conclusions of this study are provided in Sect. 5.

## 2 Material and methods

### 2.1 IASI NH<sub>3</sub> version 4 observations

IASI is an infrared Fourier transform spectrometer on board the sun-synchronous polar-orbiting MetOp-A/B/C satellites, which were respectively launched in 2006, 2012, and 2018 (Clerbaux et al., 2009). IASI has a cross-track scanning swath width of ∼ 2200 km, with a pixel size of ∼ 12 km in diameter at nadir. Each instrument on board one of the sun-synchronous satellites covers almost all locations over the globe twice a day, once at daytime and once at nighttime, with overpasses around 09:30 and 21:30 local solar time (LST), respectively. The vertical sensitivity of the IASI NH<sub>3</sub> measurements, mainly in the boundary layer where NH<sub>3</sub> is predominantly confined, varies as a function of the ther-



mal contrast between the surface and the atmospheric layers (Clarisse et al., 2010; Di Gioacchino et al., 2024). The NH<sub>3</sub> total column observations from the IASI measurements in the first version were retrieved using the so-called hyperspectral range index (HRI) in an extended spectral range (800–1200 cm<sup>−1</sup>) and using look-up tables (LUTs) built from forward radiative transfer model simulations (Van Damme et al., 2014). In the subsequent versions, an artificial neural network for the IASI (ANNI) retrieval approach was then developed and used for retrievals of IASI NH<sub>3</sub> total columns (Van Damme et al., 2017, 2021; Whitburn et al., 2016). The ANNI NH<sub>3</sub> retrieval approach uses an assumed Gaussian-shaped vertical profile of the NH<sub>3</sub> volume mixing ratio (the “prior” profile), which is modeled as a function of the altitude above the ground or ocean surface, the peak concentration altitude, and the width of the profile of significant NH<sub>3</sub> concentrations. The peak altitude over land is set at the ground surface with a width equal to the boundary layer height (Clarisse et al., 2023), as the NH<sub>3</sub> emission is generally higher near the surface and NH<sub>3</sub>-related chemistry and dispersion cause the concentration to decrease with altitude. Over the ocean, it is set to 1.4 km with a width of 0.9 km (Clarisse et al., 2023). In this study, we use daily NH<sub>3</sub> total columns from a recently released version 4 (ANNI-NH3-v4) of the IASI ANNI retrievals of NH<sub>3</sub> (Clarisse et al., 2023). The most important feature of this new ANNI-NH3-v4 data product is the introduction of the column averaging kernel (AK). The vertical AK is essential for comparison of chemistry transport model simulations against the satellite NH<sub>3</sub> retrievals, which can be used to remove the effect of the prior vertical NH<sub>3</sub> profiles used in the retrievals of the IASI NH<sub>3</sub> total columns in the model–satellite comparison. Note that the NH<sub>3</sub> distribution from IASI-ANNI-v4 is very similar to the ones with the previous version 3, although the values are about 15 %–20 % larger due to the improved setup of the HRI (Clarisse et al., 2023). Furthermore, the ANNI-NH3-v4 data product provides a more accurate characterization of the measurement uncertainty, along with several other changes, resulting in the improved temporal consistency of the IASI NH<sub>3</sub> dataset spanning from 2007 onwards (Clarisse et al., 2023).

We use daily IASI-NH3-v4 NH<sub>3</sub> global observations over land from the MetOp-B satellite from 2019 to 2022. We select only the NH<sub>3</sub> observations from the morning overpass (around 09:30 LST) because of the better precision of morning observations, as IASI is more sensitive at this time of day to the atmospheric boundary layer, where the signature of the surface emissions is higher, owing to more favorable thermal conditions. We use high-quality IASI NH<sub>3</sub> observations only with the cloud coverage lower than and equal to 10 % (Clarisse et al., 2023). We apply pre- and post-retrieval filters that accompany the dataset. The application of these filters removes respectively the observations corresponding to erroneous L1 processing of the spectra or excess cloud coverage and the observations corresponding to measurements with limited or no sensitivity to the measured quantity and

retrievals satisfying certain threshold conditions (Clarisse et al., 2023).

## 2.2 LMDZ-INCA global chemistry transport model and simulations

We use the global climate–aerosol–chemistry transport model LMDZ-INCA to simulate the global NH<sub>3</sub> concentrations, along with a state-of-the-art gas phase tropospheric chemistry scheme as well as aerosols including sulfate, nitrate, black carbon (BC), particulate organic matter (POM), dust, and sea salt. LMDZ-INCA is a coupled model based on an atmospheric general circulation model (GCM) LMDZ V6 (Laboratoire de Météorologie Dynamique) (Boucher et al., 2020; Hourdin et al., 2020), a chemistry and aerosols model INCA V6 (INteraction with Chemistry and Aerosol) (Hauglustaine et al., 2004, 2014), and a global land surface dynamical vegetation model ORCHIDEE (ORGanizing Carbon and Hydrology In Dynamic Ecosystems) (Krinner et al., 2005). The model uses a monotonic, finite-volume, second-order parameterization to calculate large-scale advection of water vapor, liquid and solid water, and tracers (Boucher et al., 2020). The model uses the “New Physics” (NP) version of the physical parameterizations, which includes a turbulent scheme based on the prognostic equation for the turbulent kinetic energy (Yamada, 1983), the “Thermal Plume Model” for the convective boundary layer (Rio and Hourdin, 2008), a parameterization for cold pools and wakes resulting from convective rainfall evaporation (Grandpeix and Lafore, 2010), and Emanuel’s deep convection parameterization scheme (Emanuel, 1991). LMDZ-INCA interactively accounts for the emissions, transport (resolved and subgrid scales), and deposition (both dry and wet) of chemical species and aerosol, and it incorporates a full chemical scheme for the NH<sub>3</sub> cycle and nitrate particle formation (Hauglustaine et al., 2014).

The LMDZ-INCA model configuration used in this study has a horizontal resolution of 1.27° latitude × 2.5° longitude with 79 hybrid  $\sigma$ -pressure levels within a terrain following vertical coordinate stretches up to 80 km. We conducted LMDZ-INCA spin-up simulations from 2010 to 2018 and then reference simulations for a period of 4 years from 2019 to 2022, which we used for the model comparison with the IASI NH<sub>3</sub> observations and for the global NH<sub>3</sub> emission inversions. The simulations were driven by nudging the GCM winds with a 3.6 h relaxation time to the 6-hourly ECMWF Reanalysis v5 (ERA5) data, regridded onto the LMDZ-INCA model grid. In the LMDZ-INCA simulations, we used the monthly global anthropogenic emission of the chemical species and gases, including NH<sub>3</sub>, from the open-source Community Emissions Data System (CEDS) global bottom-up gridded inventories (McDuffie et al., 2020), with an initial horizontal resolution of 0.5° × 0.5°, interpolated onto the model horizontal grid. We used conservative regridding by ensuring that the total mass (e.g., emis-

sions) was preserved during the interpolation. The CEDS global emission inventories provide emissions of NH<sub>3</sub>, NO<sub>x</sub>, SO<sub>2</sub>, NMVOCs, CO, OC, and BC from 11 anthropogenic sectors, including agriculture, energy, on-road and non-road transportation, residential, commercial, waste solvents, international shipping, and others (McDuffie et al., 2020). The CEDS inventory also includes emissions of NO and NH<sub>3</sub> from agricultural soils with both synthetic and manure fertilizers. Because CEDS anthropogenic emissions are available only up to 2019, the CEDS emission fluxes for the post-2019 years were developed based on the combination of the CEDS emissions in 2019 with the carbon emission growth rate from 2019 to the target year. The data on the emissions growth rate were derived from the Carbon Monitor dataset (<https://carbonmonitor.org/>, last access: 1 August 2024) and calculated by source sector, by month, and by country. This approach to extrapolate emission fluxes based on CO<sub>2</sub> data has been commonly applied to various species, particularly those associated with fossil fuel emissions. This has led to noticeable variations in emissions of species like SO<sub>2</sub> and NO<sub>x</sub>, which have been simultaneously used in the LMDZ-INCA simulations with the full chemical scheme for sulfate and nitrate particle formation (Fig. S1 in the Supplement). However, as extrapolation calculations are conducted for each source sector separately and NH<sub>3</sub> emissions mostly come from agricultural activities, which do not emit CO<sub>2</sub> directly, applying this approach to extrapolate NH<sub>3</sub> emissions for the post-2019 years resulted in almost invariant NH<sub>3</sub> emissions after 2019 (Fig. S1). While this approach may seem simplistic for NH<sub>3</sub> fluxes, it was used in this study to construct the spatial distribution of prior emissions, as we expect satellite data to drive year-to-year variations in the final inversion results. Because the anthropogenic emissions are derived from the CEDS inventory at a monthly resolution, they are uniformly distributed in time at the hourly resolution in the input to the LMDZ-INCA simulations, without incorporating diurnal cycles. We used fire emissions from the Global Fire Emissions Database (GFED4) (van der Werf et al., 2017) and biogenic volatile organic compound (VOC) emissions calculated from the ORCHIDEE vegetation model (Messina et al., 2016). Emission fluxes from anthropogenic and natural sources were prescribed to the model as monthly forcing files for different species. We sampled the simulated NH<sub>3</sub> concentration at an hourly frequency over a 4-year period from 2019 to 2022. We used these hourly LMDZ-INCA model-simulated NH<sub>3</sub> data for our analysis and inversions with IASI NH<sub>3</sub> observations from the morning overpass.

### 2.3 Model and satellite comparison approach

The retrievals of NH<sub>3</sub> total column observations,  $\Omega_{\text{obs}}$ , where “obs” stands for the “observed” IASI NH<sub>3</sub> total columns in the IASI-ANNI-NH3-v4 data product, are implicitly dependent on assumed (prior) Gaussian-shaped vertical profiles of the NH<sub>3</sub> volume mixing ratio above the land and sea surfaces

(Clarisse et al., 2023). As a result, the comparison between satellite-retrieved and model-simulated column abundances is influenced by the shape of the vertical profile of NH<sub>3</sub> mixing ratios assumed in the retrievals. The total column averaging kernel (AK), as provided in the ANNI-NH3-v4 data product, characterizes the altitude-dependent sensitivity of the retrieved atmospheric column to changes in the true profile (Eskes and Boersma, 2003). The importance of the AK in correctly comparing model simulations with the satellite observations has long been established (Cooper et al., 2020; Douros et al., 2023 for NO<sub>x</sub>; Koukouli et al., 2018 for SO<sub>2</sub>). There are several possible approaches of comparing model simulations with the satellite observations enabling the model-retrieval comparison to be independent of the assumption on the profiles used in the retrievals (Cooper et al., 2020; Douros et al., 2023; Cao et al., 2022; Ding et al., 2024). Here, we convolved the simulated LMDZ-INCA NH<sub>3</sub> vertical profiles with the IASI NH<sub>3</sub> total column AKs. The convolved LMDZ-INCA model simulation of the NH<sub>3</sub> columns,  $\Omega_{\text{mod}}$ , where “mod” stands for the “modeled” LMDZ-INCA NH<sub>3</sub> total column, is obtained by weighting the vertical integration of the model NH<sub>3</sub> sub-columns ( $x_l$ ) with the averaging kernel (AK<sub>*l*</sub>) (Clarisse et al., 2023; Eskes and Boersma, 2003):

$$\Omega_{\text{mod}} = \sum_l \text{AK}_l x_l, \quad (1)$$

where the summation over  $l$  is over the 14 vertical levels of IASI NH<sub>3</sub> retrievals (on which an assumed NH<sub>3</sub> vertical profile and AKs of retrievals are defined). Here,  $x_l$  values are obtained by interpolating LMDZ-INCA simulated original NH<sub>3</sub> mole fraction vertical profiles (at 79 levels) onto the levels corresponding to IASI-ANNI-NH3-v4 retrievals (14 levels). The interpolation is performed in a manner that conserves the NH<sub>3</sub> total column amount. The application of the AK to the simulated LMDZ-INCA NH<sub>3</sub> profiles ensures the elimination of an assumed NH<sub>3</sub> profile error contribution to the model–satellite comparison (Boersma et al., 2004; Eskes and Boersma, 2003) and that the model-simulated column is integrated in a way that reflects the retrieval sensitivity.

In order to illustrate the impact of the AK on modeled NH<sub>3</sub> total columns, Fig. 1 shows LMDZ-INCA simulated NH<sub>3</sub> mole fraction vertical profiles over a model grid cell in India on three clear-sky days (24 February, 30 March, 28 October) in 2019 and the modeled NH<sub>3</sub> sub-columns with and without application of the AKs corresponding to one of the IASI pixels in that model grid cell, obtained from the modeled NH<sub>3</sub> mole fraction profile interpolated on the vertical levels of IASI-ANNI-NH3-v4 retrievals. Despite the AK values varying relatively smoothly with altitude above the ground surface, the application of the AK can amplify modeled NH<sub>3</sub> sub-columns at higher altitudes compared to those calculated without the AK (Fig. 1). This effect is generally due to the interaction between the vertical structure of the modeled NH<sub>3</sub> vertical profile and the thickness (or pressure width) of the

sub-columns. Because each NH<sub>3</sub> sub-column represents the mass of NH<sub>3</sub> within a specific pressure layer, layers with both significant NH<sub>3</sub> concentrations and wider pressure intervals can result in larger NH<sub>3</sub> sub-column values, even if the AK is not at its peak for those layers (Fig. 1). Consequently, even modest AK values at higher altitudes, combined with substantial NH<sub>3</sub> mass in thick pressure layers, can lead to amplified contributions to the total column. The subfigures in Fig. 1 show that the LMDZ-INCA NH<sub>3</sub> local vertical profiles mostly decrease with altitude and are almost similar to the Gaussian-shaped NH<sub>3</sub> vertical profile centered at the land surface used as a prior in the IASI-ANNI-NH3-v4 retrievals. However, the model-simulated vertical NH<sub>3</sub> profiles for some days (e.g., Fig. 1b) deviate from such a general smoothed NH<sub>3</sub> vertical profile shape assumed in the IASI NH<sub>3</sub> retrievals and show secondary peak(s) at some higher altitude. Although a short-lived species like NH<sub>3</sub> largely resides within the atmospheric boundary layer and the long-term averaged NH<sub>3</sub> vertical distribution in the boundary layer or in the lower troposphere could be assumed as smoothly decreasing with the altitudes, with maximum at the land surface, high-temporal-scale NH<sub>3</sub> vertical profiles corresponding to the IASI overpass time can be a little more complex than this averaged smoothed profile, as observed in both model simulations (Fig. 1b) and aircraft- and surface-based in situ measurements (Cady-Pereira et al., 2024; Guo et al., 2021; Pu et al., 2020). This suggests a potential need to refine the assumed NH<sub>3</sub> vertical profile for more accurate satellite NH<sub>3</sub> retrievals, though the necessity for this refinement may depend on specific locations and meteorological conditions. Across all these days, the application of the AKs results in higher LMDZ-INCA NH<sub>3</sub> total column values compared to the ones without applying the AKs. The AK from the ANNI-NH3-v4 product often exhibits magnitudes exceeding unity at altitudes corresponding to the LMDZ-INCA NH<sub>3</sub> sub-column peak altitudes. This results in larger modeled NH<sub>3</sub> total column values when using the AK.

At a given hourly output of the model simulations with the IASI observations from the morning overpass around 09:30 LST, we derive a corresponding LMDZ-INCA NH<sub>3</sub> profile for each individual IASI NH<sub>3</sub> pixel within a model grid cell that contains the center of this pixel and derive the convolved LMDZ-INCA modeled NH<sub>3</sub> total column by applying the corresponding AK. Because the IASI resolution is much finer than that of LMDZ-INCA, this process yields several convolved modeled NH<sub>3</sub> total columns for a single model grid cell. We then average these resulting observed ( $\Omega_{\text{obs}}$ ) and corresponding AK-convolved modeled ( $\Omega_{\text{mod}}$ ) NH<sub>3</sub> total columns at the model spatial resolution ( $1.27^\circ \times 2.5^\circ$ ) for a proper comparison at the coarsest resolution between the two products. We exclude the grids of the averaged NH<sub>3</sub> total columns from the analysis if there are fewer than four high-quality IASI pixels within a model spatial grid or if the grid-cell average of observations is negative due to some negative IASI NH<sub>3</sub> total column retrievals.

## 2.4 Inversion of the global NH<sub>3</sub> emission from IASI observations

We use the finite difference mass-balance (FDMB) inversion approach (Cooper et al., 2017; Lamsal et al., 2011) for the global inversion of NH<sub>3</sub> emissions using NH<sub>3</sub> total columns from the LMDZ-INCA model simulations and IASI NH<sub>3</sub> observations. The inversion approach assumes that the short lifetime of NH<sub>3</sub> of a few hours to a day in the atmosphere limits its horizontal transport on coarse grids and thus implicitly conducts local analysis, deriving local surface emissions (in a given model horizontal grid cell) based on local observations (corresponding the same model horizontal grid cell), even though it relies on full 4D (3D in space, 1D in time) simulations with LMDZ-INCA. The FDMB inversion approach relies on the estimation of the local sensitivities ( $\beta$ ) of the simulations of NH<sub>3</sub> total columns to changes in the local NH<sub>3</sub> emission, addressing non-linear chemistry effects from the model simulations. It derives NH<sub>3</sub> emission estimates at each grid cell by scaling a priori NH<sub>3</sub> emission (here based on the anthropogenic emissions from the CEDS inventory), considering the local sensitivity of NH<sub>3</sub> simulations to changes in emission and the relative difference between the observed and modeled NH<sub>3</sub> total columns. Our objective is a daily estimate of 10 d running mean global anthropogenic NH<sub>3</sub> emissions over land. However, with only satellite NH<sub>3</sub> observations, it is challenging to distinguish between anthropogenic and natural sources. Therefore, our approach focuses solely on grid cells and days where and when the prior NH<sub>3</sub> emission inventory indicates that the emissions are dominated by the anthropogenic sources and where and when we have retained grid-cell averages of the IASI NH<sub>3</sub> observations (see Sect. 2.3). We use the daily combined anthropogenic NH<sub>3</sub> emissions from CEDS and fire emissions from the GFED4 inventories, which are derived from monthly data and uniformly distributed at the hourly scale within each day in the LMDZ-INCA simulations, as a priori emissions ( $E_a$ ) in the inversions. We select the grid cells with dominating anthropogenic NH<sub>3</sub> emissions by identifying those where the ratio of anthropogenic NH<sub>3</sub> emissions to total NH<sub>3</sub> emissions (including anthropogenic, biogenic, and fire NH<sub>3</sub> emissions) is greater than 0.6. This selection of dominant anthropogenic emissions slightly alters their spatial distribution over the years from 2019 onward due to variations in fire emissions across different years. We compute a 10 d running average at each grid cell of the modeled and observed NH<sub>3</sub> total columns and of the a priori emissions to smooth out the daily fluctuations in observed NH<sub>3</sub> total columns and to increase the sample size and spatial coverage of the daily flux estimates. Following Cooper et al. (2017) and Lamsal et al. (2011), for a given day and over each model horizontal grid cell, the satellite-constrained NH<sub>3</sub> emission estimates ( $E_{\text{IASI}}$ ) using the observed IASI NH<sub>3</sub> total columns ( $\Omega_{\text{obs}}$ ) and the modeled LMDZ-INCA columns convolved with the AKs ( $\Omega_{\text{mod}}$ ) corresponding to a priori NH<sub>3</sub> emis-

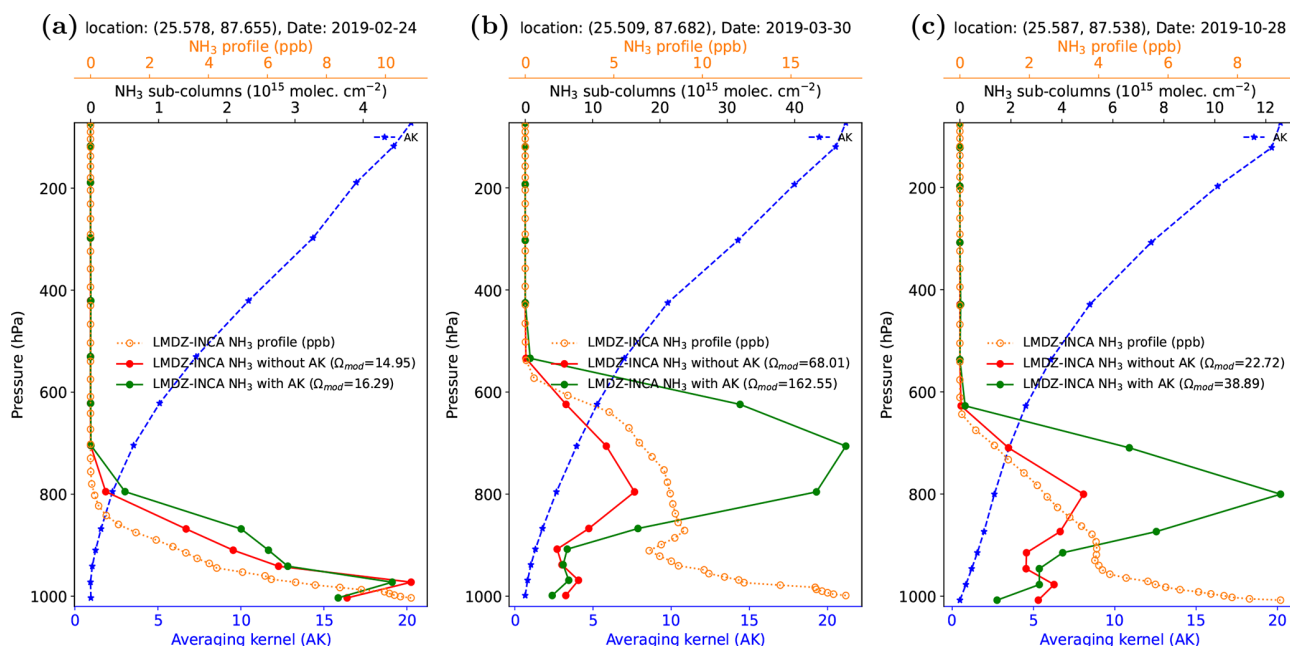


**Figure 1.** An example illustrating the convolution of LMDZ-INCA NH<sub>3</sub> vertical profiles with the IASI-ANNI-NH<sub>3</sub>-v4 averaging kernels (AK) to calculate the convolved LMDZ-INCA modeled NH<sub>3</sub> total column ( $\Omega_{\text{mod}}$ ). The LMDZ-INCA simulated original NH<sub>3</sub> mole fraction vertical profile (in ppb) at 79 model levels (represented by the orange dashed line on the secondary x axis at the top) and the AKs from individual IASI NH<sub>3</sub> pixels (represented by the blue dashed line on the primary x axis at the bottom) within a model grid cell centered at (25.5, 87.6) in India on three dates: **(a)** 24 February 2019, **(b)** 30 March 2019, and **(c)** 28 October 2019, and the corresponding NH<sub>3</sub> sub-columns (in molecules cm<sup>-2</sup>) (secondary x axis at the top) from the NH<sub>3</sub> vertical profiles simulated by LMDZ-INCA in this grid cell interpolated on the vertical levels of the assumed NH<sub>3</sub> profile in the IASI retrievals (shown in red) and the convolved LMDZ-INCA sub-column profiles with the AK (displayed in green). The values of  $\Omega_{\text{mod}}$  with and without using the AK (in molecules cm<sup>-2</sup>) are also presented on the respective sub-plots for each day.

sion ( $E_a$ ) used in the model simulations are calculated as:

$$E_{\text{IASI}} = E_a \left( 1 + \beta \frac{\Omega_{\text{obs}} - \Omega_{\text{mod}}}{\Omega_{\text{mod}}} \right), \quad (2)$$

where a unitless scaling factor  $\beta$  accounts for the local sensitivity of the modeled NH<sub>3</sub> total columns ( $\Delta\Omega_{\text{mod}}/\Omega_{\text{mod}}$ ) to perturbations of the a priori NH<sub>3</sub> emissions ( $\Delta E_a/E_a$ ) and is defined as:

$$\beta = \frac{\Delta E_a/E_a}{\Delta\Omega_{\text{mod}}/\Omega_{\text{mod}}}. \quad (3)$$

We perform two LMDZ-INCA model simulations for each year: one using the prior emissions, with the anthropogenic NH<sub>3</sub> emissions from the CEDS bottom-up inventory for the year 2019, updated for subsequent years (see Sect. 2.2), and another with a 40 % reduction in the CEDS anthropogenic NH<sub>3</sub> emissions to derive  $\beta$ . We apply some filters to  $\beta$ , to the observed and/or the modeled NH<sub>3</sub> total columns, and/or to the bottom-up emissions to select the grids corresponding to the dominating anthropogenic emissions and to avoid negative or extreme unrealistic estimates of the NH<sub>3</sub> emissions from the inversions. We select grids over land only for (i)  $0 \leq \beta \leq 10$ , (ii)  $\beta \frac{\Omega_{\text{obs}} - \Omega_{\text{mod}}}{\Omega_{\text{mod}}} \geq -1$ , and (iii)  $\Omega_{\text{mod}}$  and

$\Omega_{\text{obs}} > 1 \times 10^{15}$  molecules cm<sup>-2</sup>. Figure S2 in the supporting information shows an example of the distribution of monthly mean values of  $\beta$  for July 2019. The values of  $\beta$  are less than 1.5 over most of the major NH<sub>3</sub>-emitting land regions worldwide.

Satellite data gaps and some filters applied to observations and different variables in the FDMB inversion approach to focus on model grid cells dominated by anthropogenic NH<sub>3</sub> emissions result in numerous grids or days where NH<sub>3</sub> emissions could not be derived directly from the IASI NH<sub>3</sub> observations. Therefore, the derivation of national or regional budgets of anthropogenic emissions at daily (10 d scale) to monthly and annual scale from the satellite observations requires a proper gap-filling of grid cell or days for which the inversion protocol does not yield emission estimates. To fill these gaps in IASI-constrained NH<sub>3</sub> emissions, we use a rather conservative approach utilizing IASI-constrained NH<sub>3</sub> emissions and the corresponding a priori CEDS anthropogenic NH<sub>3</sub> emissions used in the inversions. The gap-filling is performed over some specific regions. In order to gap-fill the daily unconstrained NH<sub>3</sub> emissions, we compute a daily scaling factor as a ratio between the IASI-constrained and the corresponding CEDS anthropogenic NH<sub>3</sub> emissions integrated over a specific region. The missing emissions in



that selected region are gap-filled by multiplying for each corresponding grid cell the CEDS NH<sub>3</sub> emissions with these scaling factors. For a given day, when the spatial coverage of the IASI-constrained anthropogenic NH<sub>3</sub> emissions is less than 60 % in a specific region due to poor satellite coverage and due to other data filtering to apply the FDMB inversion approach, we apply some constraints on the scaling factor to prevent spurious gap-filled emissions. If the IASI-constrained emissions coverage is less than 10 %, we directly use the prior CEDS NH<sub>3</sub> emissions. For coverage between 10 % and 40 %, we cap the scaling factor at 1.25, and for coverage between 40 % and 60 %, we cap it at 1.5. For the gap-filling, we use 10 continental regions (illustrated in Fig. S3) over the main land worldwide as defined by Ge et al. (2022) based on 58 IPCC reference regions representing consistent regional climate features described in Iturbide et al. (2020). Ge et al. (2022) used the nine regions (except the “rest of the world” region) to access global and regional budgets and fluxes of atmospheric reactive N and S gases and aerosols. The fraction of the IASI-constrained and the gap-filled NH<sub>3</sub> emissions per season across six regions for each year from 2019 to 2022 in Fig. S4 shows that the gap-filling of emissions over most of the regions is mostly higher during winter and minimum during spring. However, in some regions such as India and Africa, the percentage of the gap-filled emissions to the total seasonal emissions is higher in summer compared to other seasons due to relatively smaller numbers of satellite observations, caused by higher cloud coverage during the monsoon season. The overall percentage of the gap-filled NH<sub>3</sub> emissions to the total emissions worldwide is maximum (up to  $\sim 28$  %) during winter and minimum (up to  $\sim 11$  %) during spring, and it ranges from  $\sim 16$  % to 19 % during summer and autumn (Fig. S4). However, because the attribution of the NH<sub>3</sub> emissions in winter to the total annual emissions is smaller compared to the other seasons, the total gap-filled emissions in winter are still lower than in the other seasons (Fig. S5).

### 3 Results

We present the results from the LMDZ-INCA model comparisons with satellite NH<sub>3</sub> observations and inversions of NH<sub>3</sub> emissions at both global and regional scales over land areas. For regional analysis, we select six major NH<sub>3</sub> source regions: India, China, Africa, Europe, North America, and South America (Fig. S6). We present and discuss our results across various temporal scales, ranging from daily to monthly, seasonal, and annual.

#### 3.1 Model and satellite comparison of NH<sub>3</sub> total columns

We start by comparing the LMDZ-INCA model-simulated NH<sub>3</sub> total columns driven by the prior emissions and convolved with the AKs against the IASI NH<sub>3</sub> observations, with first a worldwide overview and then some focuses on regions over land. In addition to assessing global and regional mean comparisons between the modeled and the observed IASI NH<sub>3</sub> columns, we also calculate the Pearson's correlation coefficient ( $r$ ) and root mean square error (RMSE) between the annual or monthly mean simulated and observed values at the model grid level as part of our comparative analysis (shown in Figs. 2 and 3 for 2019 and Fig. S7 for all years from 2019 to 2022).

Figure 2 compares the annual mean modeled LMDZ-INCA NH<sub>3</sub> columns ( $\Omega_{\text{mod}}$ ) with the observed IASI NH<sub>3</sub> column retrievals ( $\Omega_{\text{obs}}$ ) regridded on the LMDZ-INCA model grid ( $1.27^\circ \times 2.5^\circ$ ) worldwide over land for the year 2019 (Fig. S7 for all 4 years from 2019 to 2022). It shows that the annual mean worldwide spatial distributions of the modeled NH<sub>3</sub> columns are approximately similar to those of the IASI NH<sub>3</sub> retrievals and that there is a good spatial correlation ( $r = 0.71$ ) between them. However, the IASI NH<sub>3</sub> observations indicate higher NH<sub>3</sub> abundance compared to the LMDZ-INCA simulations across most of the regions worldwide, except over the South Asia and Eastern Siberia regions (Fig. 2). We observe an overall underestimation of the global annual mean LMDZ-INCA NH<sub>3</sub> columns  $\Omega_{\text{mod}}$  (mean:  $0.33 \times 10^{16}$  molecules cm<sup>-2</sup>) compared with the observed IASI retrievals  $\Omega_{\text{obs}}$  (mean:  $0.54 \times 10^{16}$  molecules cm<sup>-2</sup>). The RMSE between the annual mean gridded  $\Omega_{\text{mod}}$  and  $\Omega_{\text{obs}}$  worldwide is  $0.52 \times 10^{16}$  molecules cm<sup>-2</sup>.

Emphasizing the regional analysis, in Fig. 3, we found that the modeled NH<sub>3</sub> total columns are lower than the IASI NH<sub>3</sub> observations over most of the selected regions, except over the Indian region (also Southeast Asia, not shown; see Fig. 2), and also over a region in Eastern Siberia, where the model shows an overestimation of the observations (not shown, but see Fig. 2). The annual regional mean of monthly  $\Omega_{\text{mod}}$  over the China, Africa, Europe, South America, and North America regions are respectively  $\sim 4$  %,  $\sim 52$  %,  $\sim 53$  %,  $\sim 58$  %, and  $\sim 70$  % smaller compared to  $\Omega_{\text{obs}}$  (Fig. 2). However, over the Indian region, the annual regional mean of  $\Omega_{\text{mod}}$  is  $\sim 44$  % larger than  $\Omega_{\text{obs}}$ . The monthly regional mean time series of the IASI NH<sub>3</sub> observations in Fig. 3 show that the NH<sub>3</sub> columnar abundance over most of the regions is higher during spring and/or summer months compared than in winter. These elevated NH<sub>3</sub> columns observed during spring and/or summer months compared to winter months can be attributed to increased agricultural activities, particularly the prominent use of N-fertilizers in crops during warmer seasons. High NH<sub>3</sub> concentrations are also influenced by temperature, as warmer

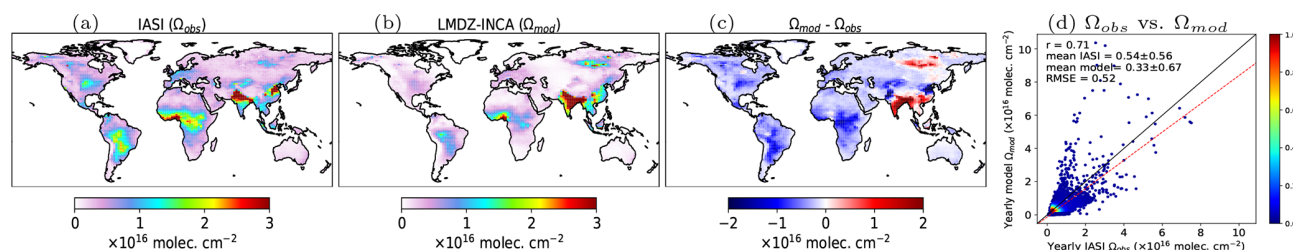


**Figure 2.** The spatial distributions of the annual mean  $\text{NH}_3$  total columns (in molecules  $\text{cm}^{-2}$ ) for the year 2019 (a) from the IASI-ANNI- $\text{NH}_3$ -v4 observations ( $\Omega_{\text{obs}}$ ) and (b) from LMDZ-INCA model-simulated columns after applying the averaging kernel ( $\Omega_{\text{mod}}$ ), as well as (c) the difference ( $\Omega_{\text{mod}} - \Omega_{\text{obs}}$ ) between them. The last column (d) shows the scatter density plots between these annual mean observed IASI and the corresponding LMDZ-INCA model  $\text{NH}_3$  columns across all model grid cells worldwide over land. In the scatter plots, the solid black line represents the one-to-one line, while the dashed red line represents the regression line.

temperatures can enhance  $\text{NH}_3$  volatilization from soils and agricultural surfaces (Sutton et al., 2013). This synergistic effect of agricultural practices and temperature contributes to the seasonal variation in  $\text{NH}_3$  emissions, with higher concentrations during spring and/or summer months.

The monthly regional mean modeled  $\text{NH}_3$  columns in Fig. 3 mostly follow the seasonal variation of the IASI observations over the South American and African regions, as well as over the European region to some extent. However, for other remaining regions, especially over the Indian, Chinese, and Middle East (not shown) regions, the seasonality of the modeled  $\text{NH}_3$  columns largely deviates from the observations, and we see a large scatter between the monthly mean gridded modeled and observed  $\text{NH}_3$  columns (Fig. 3a and b). Over the Indian region, the model shows two main peaks, with the highest peak in May following a secondary smaller peak in September, whereas the IASI observations show the highest peak in July and a smaller one in April (Fig. 3a1). The high  $\text{NH}_3$  loading from the IASI observations over the Indian region from June to August with a maximum peak in July and a secondary, much smaller peak in April (Fig. 3a1) is consistent with the cropping cycle (Kuttippurath et al., 2020), high usage of the N-fertilizers, and high temperature during these monsoon and summer months in the Indo-Gangetic Plain (IGP) region spanning the banks of the Indus and Ganges rivers and their tributaries (Beale et al., 2022). However, as mentioned before, the variation and two distinct peaks in the modeled  $\text{NH}_3$  columns is similar to the variation and peaks in the anthropogenic  $\text{NH}_3$  emissions used in the model simulations (Fig. 3). Similarly, over the Chinese region, the observed  $\text{NH}_3$  columns show the highest peak in July, which is not captured by the simulations that show the maximum peak in May, followed by a small peak in September. In these regions, because of differences in seasonal variations between the modeled and observed  $\text{NH}_3$  columns, we see weak spatial correlations between the monthly mean observed and modeled gridded  $\text{NH}_3$  columns (Fig. 3) that are smaller than in other regions like Africa, South America, and Europe, where the seasonality in both the modeled and observed  $\text{NH}_3$  total columns is roughly similar.

Figure 3 also shows the seasonal cycles in the regional anthropogenic (CEDs) and fire (GFED4) emissions from the global emission inventories used in the model simulations. Over some regions like South America, North America, and Africa, fire-related  $\text{NH}_3$  emission has a visible contribution to this seasonal variation in total emissions, whereas over the India, China, and European regions, this attribution is very small (Fig. 3). This finding shows that the seasonality in the modeled  $\text{NH}_3$  total columns mostly varies with the seasonality in the combined anthropogenic and fire-related  $\text{NH}_3$  emissions over these regions (Fig. 3). Therefore, the seasonality differences between the model and observations over some regions are mostly due to the different seasonality embedded in the prior  $\text{NH}_3$  emissions used for the model simulations (Fig. 3). The model comparison analysis for other years from 2020 to 2022 shows a similar behavior of the modeled and observed  $\text{NH}_3$  columns. Notably, the seasonality of anthropogenic  $\text{NH}_3$  emissions in the CEDs inventory is mainly derived according to the European agricultural practices based on the ECLIPSE v5 model, which leads to  $\text{NH}_3$  emission peaks mostly in May and September corresponding to the application of fertilizers before planting and after harvesting the crops (Beale et al., 2022). However, this seasonal variation of the  $\text{NH}_3$  emissions in CEDs may not accurately reflect the diverse agricultural practices in other regions like India, China, and the Middle East (Fig. 3) (Beale et al., 2022; Chen et al., 2023a; Kuttippurath et al., 2020). This is clearly evident from the large difference in the seasonal variations between the IASI  $\text{NH}_3$  observations and LMDZ-INCA model simulations over these regions, as the model is dominantly driven by the CEDs anthropogenic  $\text{NH}_3$  emissions in these regions (Fig. 3). This dependency on European seasonality in CEDs inventory  $\text{NH}_3$  emissions for other major agricultural  $\text{NH}_3$ -emission regions with diverse agricultural practices, like India and China, requires region-specific data to improve the accuracy of emission inventories. For some regions like South America, Africa, and North America, the observed IASI  $\text{NH}_3$  total columns show high values during specific periods, which is mainly attributed to the heightened  $\text{NH}_3$  loading resulting from biomass burning from wildfires

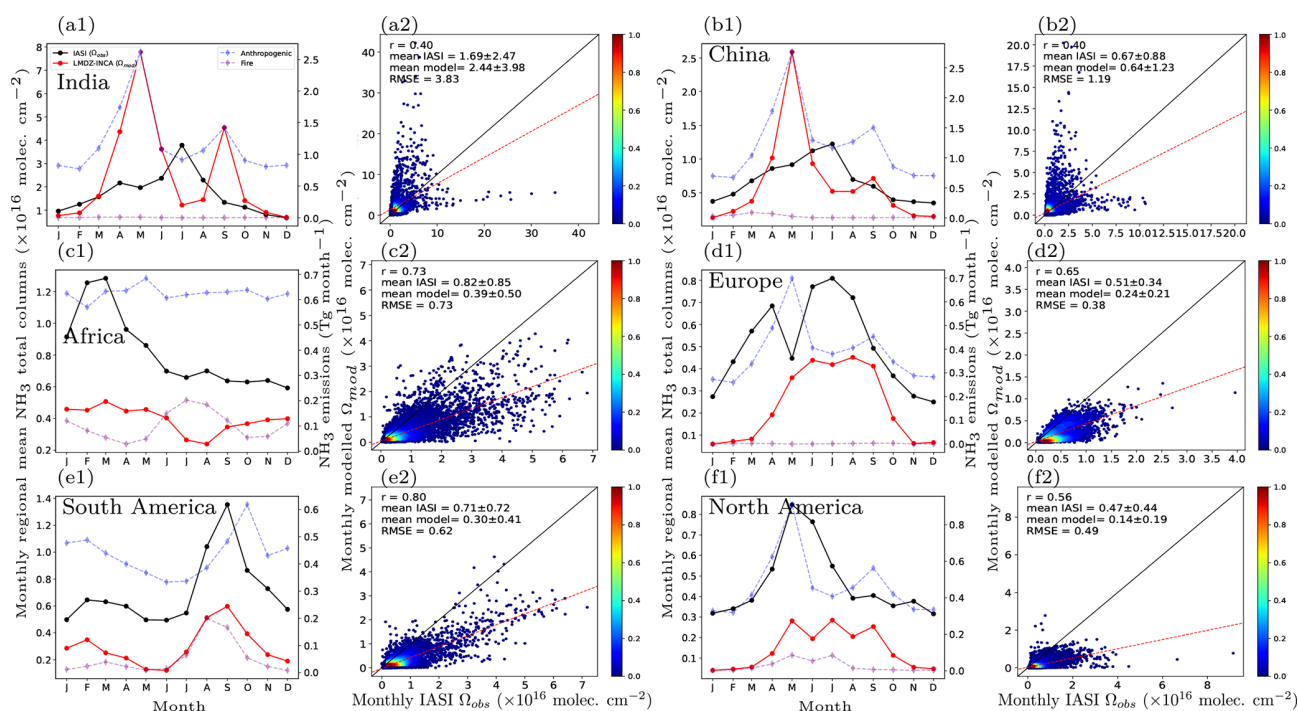


**Figure 3.** The monthly regional mean time series of the observed IASI NH<sub>3</sub> total columns ( $\Omega_{\text{obs}}$ ), the corresponding LMDZ-INCA modeled columns ( $\Omega_{\text{mod}}$ ) (primary y axis), and the monthly anthropogenic (CEDS) and fire (GFED4) NH<sub>3</sub> emissions (secondary y axis) from bottom-up inventories used in the model simulations for the year 2019 for different selected regions: **(a)** India, **(b)** China, **(c)** Africa, **(d)** Europe, **(e)** South America, and **(f)** North America (first column). The second column in each subfigure shows the scatter density plots between the monthly mean gridded observed IASI and the corresponding modeled NH<sub>3</sub> total columns over the land grid cells at  $1.27^\circ \times 2.5^\circ$  resolution in each region. In the scatter plot, the solid black lines represent the one-to-one line, while the dashed red lines represent the regression line.

in these regions. The underestimation and/or distinct seasonality of the modeled NH<sub>3</sub> columns compared to the observed IASI NH<sub>3</sub> retrievals over different regions indicate biases and/or differential seasonality in the prior NH<sub>3</sub> emissions from the inventories over these regions.

Previous validation studies of earlier IASI ANNI NH<sub>3</sub> retrieval products (e.g., with version 3) showed relatively good agreement with in situ and FTIR measurements (Guo et al., 2021; Wang et al., 2020). Although, the IASI-ANNI-NH<sub>3</sub>-v4 product introduces important improvements compared to the earlier versions and expects minimal biases, a comprehensive validation of this version has not yet been conducted, though such a validation is anticipated in upcoming studies (Clarisse et al., 2023). Therefore, the bias between the IASI NH<sub>3</sub> columns and LMDZ-INCA model simulations mainly reflects an underestimation of agricultural NH<sub>3</sub> emissions in the prior CEDS inventory, as well as a misrepresentation of their seasonal variation, particularly in the major agricultural regions. These limitations in the prior CEDS NH<sub>3</sub> emissions propagates into the model-simulated NH<sub>3</sub> columns. However, the elevated NH<sub>3</sub> columns observed by IASI during non-growing seasons in regions such as Europe and North America may also be influenced by retrieval uncertainties related to surface temperature effects and low thermal contrast.

Therefore, we cannot fully rule out remaining retrieval uncertainties in the absence of comprehensive validation of this version of the IASI NH<sub>3</sub> retrievals.

### 3.2 Evaluation of the estimated NH<sub>3</sub> emissions derived from inversions with the IASI NH<sub>3</sub> observations

In order to validate our atmospheric inversion approach (more specifically, to validate the linear approximation of the atmospheric chemistry model based on a single perturbed emission simulation) and strengthen our confidence in the NH<sub>3</sub> emission estimates, we have conducted a LMDZ-INCA model simulation using the IASI-constrained NH<sub>3</sub> emission estimates derived from our global inversions for the year 2019 and compared the simulated NH<sub>3</sub> total columns with the IASI NH<sub>3</sub> total column observations. As the current LMDZ-INCA model framework only reads NH<sub>3</sub> emissions at monthly resolution and uniformly distributes them across hours without incorporating diurnal or day-to-day variability (see Sect. 2.2), our model simulation for this evaluation uses the monthly average of the daily (at 10 d scale) inversion estimates rather than 1 d resolution inputs. However, this does not limit our capability to evaluate the inversion estimates based on comparisons to monthly and annual averages of the observations.

At the annual scale globally, the spatial correlation coefficient ( $r$ ) between the yearly mean model-simulated NH<sub>3</sub> total columns over the model horizontal land grid cells at  $1.27^\circ \times 2.5^\circ$  resolution and corresponding IASI NH<sub>3</sub> observations improve from 0.71 (using prior emissions) to 0.90 (using IASI-constrained NH<sub>3</sub> emissions), while the RMSE decreases by  $\sim 29\%$  from  $0.52 \times 10^{16}$  to  $0.37 \times 10^{16}$  molecules cm<sup>-2</sup> (Fig. S8a). Similarly, at the monthly scale globally, the  $r$  value and RMSE between the model simulations with the IASI-constrained NH<sub>3</sub> emissions and the IASI observations improve from 0.51 (using prior emissions) to 0.83 (using IASI-constrained NH<sub>3</sub> emissions), while the RMSE decreases by  $\sim 34\%$  from  $0.88 \times 10^{16}$  to  $0.58 \times 10^{16}$  molec. cm<sup>-2</sup> (Fig. S8b). The LMDZ-INCA simulation driven by the IASI-constrained NH<sub>3</sub> emissions reduces the mean fractional bias (FB) globally from  $-0.87$  to  $-0.37$  at the annual scale and from  $-1.07$  to  $-0.63$  at the monthly scale, compared to the simulation using the prior CEDS NH<sub>3</sub> emissions (Fig. S8).

At the monthly scale and across major NH<sub>3</sub> regions, including India, China, Africa, Europe, South America, and North America, the spatial correlation coefficients ( $r$ ) and RMSE between the model simulations with estimated NH<sub>3</sub> emissions from inversions and the IASI observations are respectively much higher and smaller than when the simulations are based on the prior CEDS anthropogenic NH<sub>3</sub> emissions (Fig. 4). The spatial correlation coefficient ( $r$ ) between the monthly mean IASI-constrained NH<sub>3</sub> emissions' model simulations of the NH<sub>3</sub> total columns over the model horizontal land grid cells at  $1.27^\circ \times 2.5^\circ$  resolution and the corresponding IASI NH<sub>3</sub> observations exceeds  $\sim 0.8$  in most of the regions for this 2019 validation analysis (Fig. 4). In one of the major NH<sub>3</sub>-emission regions, i.e., India, at the monthly scale, the spatial correlation increases from 0.40 to 0.86, and RMSE reduces by  $\sim 50\%$  from  $3.83 \times 10^{16}$  to  $1.91 \times 10^{16}$  molec. cm<sup>-2</sup> (Fig. 4). Similarly, over another major NH<sub>3</sub>-emission region, i.e., China, at the monthly scale, the spatial correlation increases from 0.40 to 0.79, and RMSE reduces by  $\sim 27\%$  from  $1.19 \times 10^{16}$  to  $0.87 \times 10^{16}$  molec. cm<sup>-2</sup> (Fig. 4). These findings demonstrate the general improvement brought about at different spatiotemporal scales by the update of the emission estimates from our inversions and thus the internal consistency of our global inversion framework despite the rather simple linearization of the chemistry transport underlying it. This improvement of the fit to the IASI NH<sub>3</sub> observations is a strong indication of the robustness of our inversion-based estimate of the global NH<sub>3</sub> emissions. The FB metric quantitatively confirms bias reduction in the modeled NH<sub>3</sub> columns regionally when using IASI-constrained NH<sub>3</sub> emissions in the model simulation compared to the prior CEDS NH<sub>3</sub> emissions (Fig. S9). Specifically, we observe a clear decrease in FB across all regions, except for India. In the case of India, although the FB remains slightly elevated, the RMSE shows substantial improvement, indicating better representation of the magnitude and the spa-

tial and temporal variability, even if the mean offset is not fully corrected from our inversion estimates.

### 3.3 IASI-constrained NH<sub>3</sub> emissions

In the subsequent subsections, we present and discuss the gap-filled global daily (10 d scale) NH<sub>3</sub> emission estimates integrated on different temporal and spatial scales. Over the 4-year period of our emission estimates, we present global and regional annual budgets, including the mean emissions over this period, with the range defining minimum and maximum annual emissions, as well as the variation of the regional estimates at different temporal scales ranging from daily (10 d scale) to monthly, seasonal, and annual.

#### 3.3.1 Global annual NH<sub>3</sub> emissions

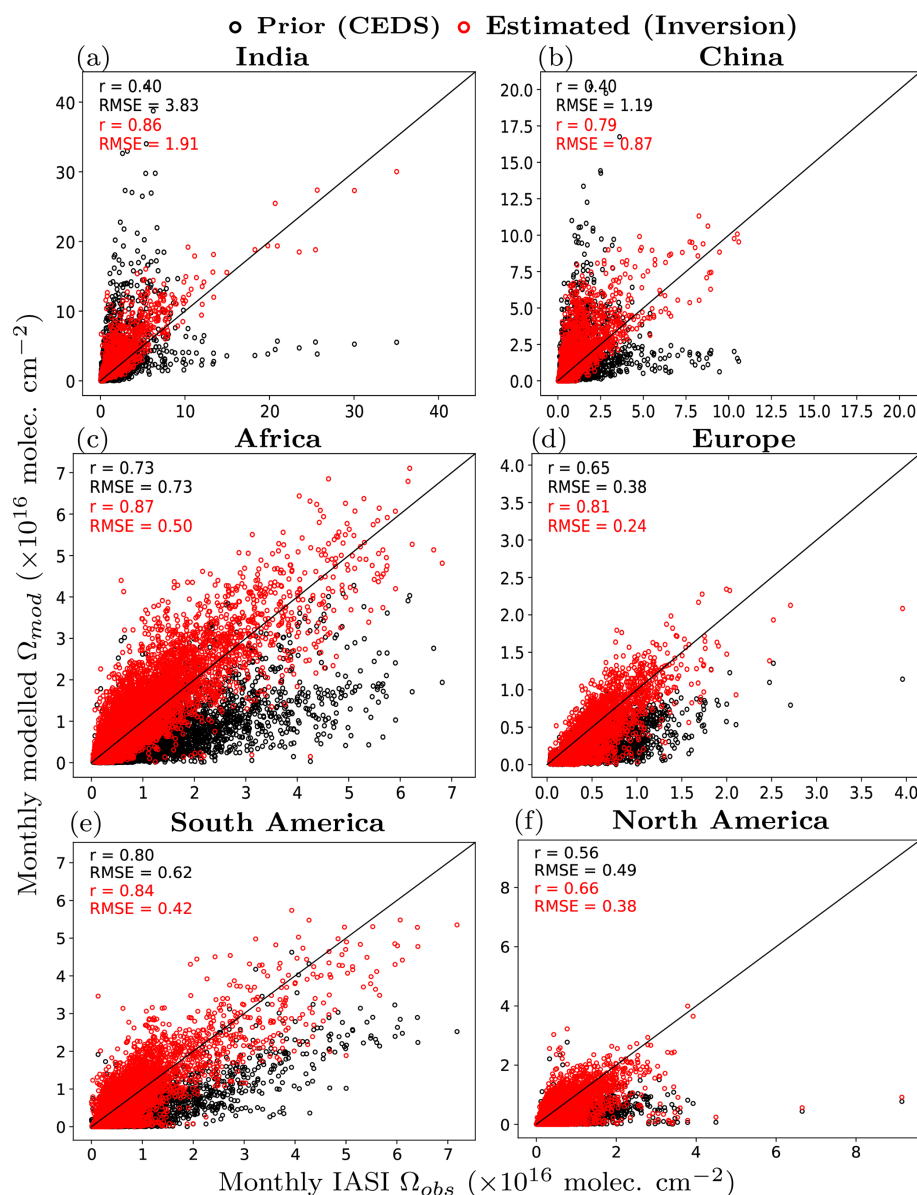
The spatial distribution of the IASI-constrained annual NH<sub>3</sub> emissions averaged over the 4-year period (2019–2022) in Fig. 5 (Fig. S10 for each year from 2019 to 2022) clearly reveals the main hotspots of the high anthropogenic NH<sub>3</sub> emissions over the globe on land areas. Figure 5 shows that the 4-year-averaged annual IASI-constrained NH<sub>3</sub> emissions have a similar spatial distribution to the prior CEDS anthropogenic NH<sub>3</sub> emissions. However, over most of the major NH<sub>3</sub>-emitting regions over the globe and over land areas, the IASI-constrained NH<sub>3</sub> emissions are higher compared to the prior CEDS emissions (Fig. 5). This finding shows that the South and East Asian regions are the highest anthropogenic NH<sub>3</sub>-emitting regions over the globe.

Figure 6 presents the global annual IASI-constrained NH<sub>3</sub> emissions and a comparison with the prior CEDS anthropogenic NH<sub>3</sub> emissions for all 4 years from 2019 to 2022. The slight differences in the prior CEDS emissions over the 4 years are mainly due to the different coverages of the dominating anthropogenic NH<sub>3</sub> emissions based on the CEDS anthropogenic and GFED fire emissions (see Sect. 2.4). For each year, the IASI-constrained NH<sub>3</sub> emissions are higher than the prior CEDS emissions. The average of the global annual NH<sub>3</sub> emission estimates over the 4-year period is  $\sim 97$  (93.8–99.9) Tg yr<sup>-1</sup>, which is  $\sim 61\%$  (55%–65%) higher than the prior CEDS anthropogenic NH<sub>3</sub> emissions. The global annual NH<sub>3</sub> emission estimates show an increasing trend from the year 2019 to 2021 (Fig. 6). However, NH<sub>3</sub> emission estimates for 2022 ( $\sim 96$  Tg yr<sup>-1</sup>) are lower than those for 2020 and 2021, though still higher than those for 2019 ( $\sim 94$  Tg yr<sup>-1</sup>).

#### 3.3.2 Regional NH<sub>3</sub> emissions and seasonal variation

Figure 7 illustrates the daily (at 10 d scale) variation of estimated NH<sub>3</sub> emissions for 4 years from 2019 to 2022 over the six specific regions, i.e., India, China, Africa, Europe, North America, and South America (defined in Fig. S6), which have the major anthropogenic ammonia emissions. In this





**Figure 4.** Comparison of the monthly averages of the gridded IASI  $\text{NH}_3$  column observations ( $\Omega_{\text{obs}}$ ) over the model horizontal land grid cells at  $1.27^\circ \times 2.5^\circ$  resolution to the corresponding averages of these observations with two simulations of LMDZ-INCA ( $\Omega_{\text{mod}}$ ) using the IASI-constrained  $\text{NH}_3$  emission estimates derived from our global inversions (red) and using the prior CEDS  $\text{NH}_3$  emissions (black) over different regions for the year 2019. Each panel shows the correlation coefficient ( $r$ ) and root mean square error (RMSE) between modeled (from both prior and IASI-constrained  $\text{NH}_3$  emissions from inversions) and observed IASI  $\text{NH}_3$  columns. The black line denotes the one-to-one line.

figure, the prior CEDS anthropogenic  $\text{NH}_3$  emissions of the year 2019 over the globe and over land areas are almost the same in magnitude and seasonal variation across the 4 years (Fig. 6), and thus the representation is shown only for the year 2019. Figure 8 shows the spatial distributions of the 4-year-averaged annual IASI-constrained  $\text{NH}_3$  emissions and the prior CEDS emissions over the six regions. The budgets of the regional annual estimated and prior  $\text{NH}_3$  emis-

sions over the 4-year period for these selected regions are presented in Fig. 9.

The Indian and Chinese regions in the South and East Asia are the major anthropogenic ammonia-emitting regions in the world, with a majority of emissions originating from large crop-specific agriculture activities, including the use of synthetic fertilizers, manure, and emissions from soils and livestock. Over the Indian region, the highest  $\text{NH}_3$  emission is from the Indo-Gangetic Plain region, which is attributed to

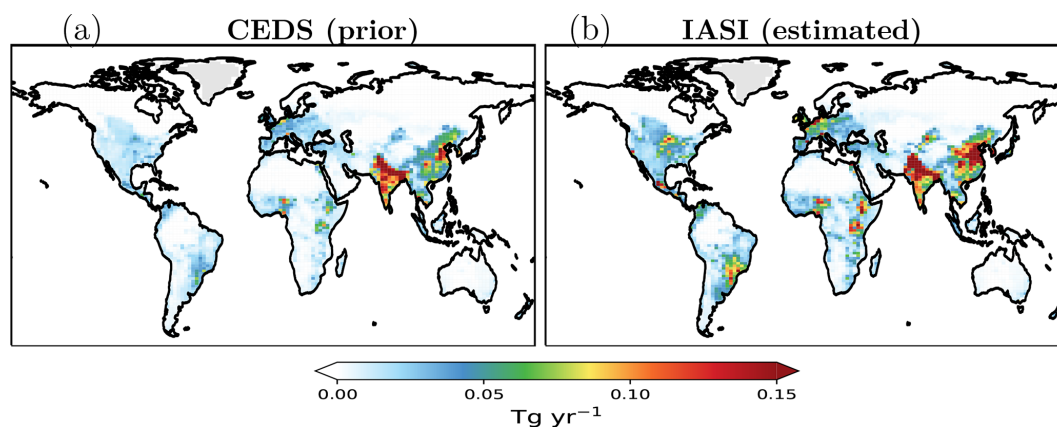


**Figure 5.** Spatial distribution of the 4-year (2019–2022) averaged annual  $\text{NH}_3$  emissions, showing (a) the prior CEDS anthropogenic  $\text{NH}_3$  emissions and (b) the IASI-constrained estimated  $\text{NH}_3$  emissions from our global atmospheric inversions.

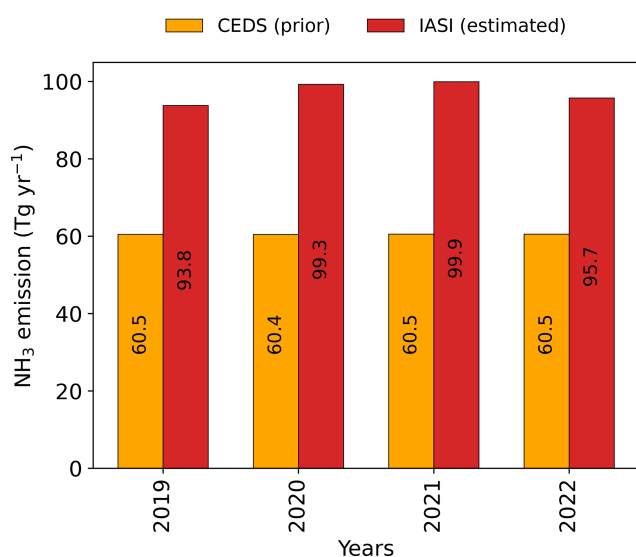


**Figure 6.** Global annual  $\text{NH}_3$  emissions for each year from 2019 to 2022, showing the prior CEDS anthropogenic  $\text{NH}_3$  emissions (orange) and IASI-constrained (red)  $\text{NH}_3$  emissions from inversions.

the intensive agriculture practices (Fig. 8a). The average annual  $\text{NH}_3$  emission estimate for the 4-year period over the Indian region is  $\sim 15.0$  ( $14.4$ – $15.4$ )  $\text{Tg yr}^{-1}$ , which is  $\sim 7\%$  ( $\sim 2\%$ – $10\%$ ) higher than the prior CEDS anthropogenic  $\text{NH}_3$  emissions ( $\sim 14.1$   $\text{Tg yr}^{-1}$ ). The annual estimates over the Indian region show a slowly decreasing trend over the 4-year period (Fig. 9a). Notably, the seasonal variations of the estimated  $\text{NH}_3$  emissions across all 4 years are similar to each other; however, they are always different from the prior CEDS  $\text{NH}_3$  emissions (Fig. 7a). The seasonal variation in  $\text{NH}_3$  emissions across different regions in the CEDS inventory dataset is rather coarse (Beaudor et al., 2023) and mostly based on the European practices of agricultural activities (Beale et al., 2022). The CEDS  $\text{NH}_3$  emissions show

two peaks, one in May and one in September, whereas the estimates show the main peak in July and August and some small peaks from January to April for each inversion year. The high  $\text{NH}_3$  emission estimates over the Indian region for July–August with a peak in July are consistent with the cropping cycle (mainly rice cultivation followed by corn), high usage of N-fertilizers, and high temperature during these monsoon and summer months in the Indo-Gangetic Plain region. The high estimates in the winter and spring months can be attributed to the usage of N-fertilizers during the winter and spring crop seasons, particularly from the predominant wheat cultivation. Biomass burning is also a small contributing source of  $\text{NH}_3$  emissions in this region, with the majority of fires resulting from crop residue and stubble burning in the spring and autumn before replanting. Therefore, there should not be a significant problem of attribution between the anthropogenic and biomass burning emissions here.

The majority of IASI-constrained and prior CEDS anthropogenic  $\text{NH}_3$  emissions over the Chinese region are confined to the East China region (Fig. 8b). The 4-year average of inverted annual  $\text{NH}_3$  emission over the Chinese region is  $\sim 23.4$  ( $22.3$ – $24.9$ )  $\text{Tg yr}^{-1}$  (Fig. 9b). This averaged IASI-constrained  $\text{NH}_3$  emission is  $\sim 62\%$  ( $\sim 54\%$ – $72\%$ ) higher than the prior CEDS emissions ( $\sim 14.5$   $\text{Tg yr}^{-1}$ ) used in the inversions. For this region, we see an increasing trend in the estimated ammonia emissions from 2019 to 2021 (Fig. 9b). The annual  $\text{NH}_3$  emission estimate for 2022 ( $23.2$   $\text{Tg yr}^{-1}$ ) is lower than those for the maximum in 2021 ( $\sim 24.9$   $\text{Tg yr}^{-1}$ ), comparable to those in 2020 ( $\sim 23.3$   $\text{Tg yr}^{-1}$ ); however, it remains higher than those for 2019 ( $\sim 22.3$   $\text{Tg yr}^{-1}$ ) (Fig. 9b). A majority of the ammonia emissions in this region originate from the crop-specific agriculture activities, more specifically the applications of synthetic fertilizer and livestock manure in different crop cultivations (Xu et al., 2018). The daily (at 10 d scale) variation of the  $\text{NH}_3$  emissions in Fig. 7b shows a strong seasonality in the estimates across all years over this region. The seasonality in the emission estimates

across all years is different from the prior CEDS NH<sub>3</sub> emissions used in the inversions. We observe mainly two high peaks in the estimates, one in spring (March–April) and one in summer (June–July), whereas the CEDS emissions show a peak in May and another in September. The NH<sub>3</sub> emission estimates also show a small third peak in October for inversion years from 2020 to 2022, except for 2019. The strong seasonality in the emission estimates in this region agrees well with the crop cycle when wheat cultivation dominates in spring and rice cultivation in the summer months (Xu et al., 2018).

As discussed before in Sect. 3.1, seasonality in the CEDS inventory NH<sub>3</sub> emissions for most of the regions is mostly based on European agricultural practices, corresponding to the application of fertilizers before planting and after harvest (Beale et al., 2022). This does not accurately capture the NH<sub>3</sub> emissions in regions like China, India, and the Middle East, where agriculture practices differ significantly (Beale et al., 2022; Chen et al., 2023a; Kuttippurath et al., 2020). By contrast, our inversion estimates based on the satellite data show more realistic seasonality of NH<sub>3</sub> emissions across different regions, closely aligning with their respective crop and agriculture cycles.

The South America, Africa, and North America regions are fire-dominated regions, particularly during the dry season, when wildfires are prevalent (Fig. S11) (Chen et al., 2023b). The biomass burning from the wildfires plays a significant role in contributing to the total ammonia emissions in these regions. For example, over the 4-year study period, biomass burning NH<sub>3</sub> emissions from GFED contribute  $\sim 11\%$ – $15\%$  in South America,  $\sim 15\%$ – $17\%$  in Africa, and  $\sim 5\%$ , with a high peak of  $\sim 26\%$  in 2021, in North America relative to the anthropogenic NH<sub>3</sub> emissions from the CEDS inventory. When fire emissions attribution in the prior emissions used for inversion is inaccurate, the predominant anthropogenic emission grids are misrepresented. In contrast, the IASI NH<sub>3</sub> observations will indicate high NH<sub>3</sub> emissions over these grid cells due to biomass burning. The recent release of the fifth version of the Global Fire Emissions Database (GFED5) indicates a 61 % increase in global burned area compared to GFED4 (Chen et al., 2023b). This increase may result in anthropogenic NH<sub>3</sub> grids from the inversions corresponding to biomass burning grids, consequently revealing heightened predominant anthropogenic NH<sub>3</sub> emission estimates over these regions due to a non-local contribution from transport from neighboring predominant biomass burning grids. Biomass burning generates NH<sub>3</sub> advection at higher altitudes, which also breaks our assumption of weak lateral transport in the FDMB inversion approach, possibly attributable to large errors in the emission estimates over these regions.

For the South American and African regions, our inversions respectively provide  $\sim 11.1$  ( $\sim 9.8$ – $12.3$ ) Tg yr<sup>−1</sup> (Fig. 8e) and  $\sim 14.4$  ( $\sim 13.8$ – $15.0$ ) Tg yr<sup>−1</sup> (Fig. 9c) of the annual NH<sub>3</sub> emissions averaged over the 4-year period.

These averaged annual estimates for these regions exceed the prior CEDS emissions by approximately 2.1 and 2 times, respectively. Our estimates show a clear increasing trend in annual NH<sub>3</sub> emission over Africa (Fig. 9c). However, a decreasing trend of annual NH<sub>3</sub> emissions from 2020 to 2022 is observed over the South American region (Fig. 9e). For the South American region, we observe a high peak in the estimated emissions during September to October in each year, and this peak in the year 2020 is much higher than that from other years (Fig. 7e). In fact, the peak in 2021 is higher than the one from the estimates in 2019 and 2022. The seasonality of the estimates over the South American region is similar to the prior CEDS anthropogenic NH<sub>3</sub> emissions (Fig. 7e). There was a large increase in the number of fires in 2020 compared to other years in this region (Fig. S11a), which can also be observed from an enhanced observed NH<sub>3</sub> loading from IASI observations over this region in these years (Fig. S7). The highest peak in the estimated NH<sub>3</sub> emissions in 2020 is mainly because of the contribution from the relatively higher number of fire occurrences in this year. For the African region, the prior CEDS NH<sub>3</sub> emissions show almost a flat seasonality relative to the estimates, with a small peak in May, whereas the estimates show at least two clear peaks: in February–March and in July–August (Fig. 7c). The NH<sub>3</sub> emissions over this region remain high during other seasons also (Fig. 7c). Although we exclude grids dominated by the biomass burning emissions based on the GFED4 bottom-up inventory in our inversions, mitigating their influence on the inversion estimates is challenging. This is due to the complexity arising from the fact that bottom-up NH<sub>3</sub> emissions lack the most updated information on fire occurrences, and the transport from biomass burning areas can extend to other regions, which is not accounted for in our inversion approach (Chen et al., 2023b).

We estimate  $\sim 12.4$  (11.6–13.4) Tg yr<sup>−1</sup> 4-year-averaged annual NH<sub>3</sub> emissions over the North American region, which is approximately 2.2 times higher than the prior CEDS anthropogenic NH<sub>3</sub> emissions (Fig. 9f). Our inversion estimates show an increasing trend of annual NH<sub>3</sub> emissions from 2019 to 2021 over this region, but the 2022 estimates are smaller than those from 2020 and 2021 and comparable to the 2019 emissions (Fig. 9f). The estimates show a strong seasonality, with peak emissions in April–May across all years (Fig. 7f). For the years 2020 to 2022, especially for 2020 and 2021, we observe a secondary peak during August and September, which is less visible in the 2019 emissions. The high secondary peak in 2020 and 2021 may result from increased biomass burning due to more wildfires in these years compared to 2019. Similar to the South American and African regions, in the North American region, the impact of biomass burning from fires from some regions may contribute to the higher ammonia emissions (Fig. S11c). In fact, the highest peak in the estimated emissions in 2020 in this region corresponds to an extreme cluster of wildfire events known as the “August Complex Fire”. This event originated

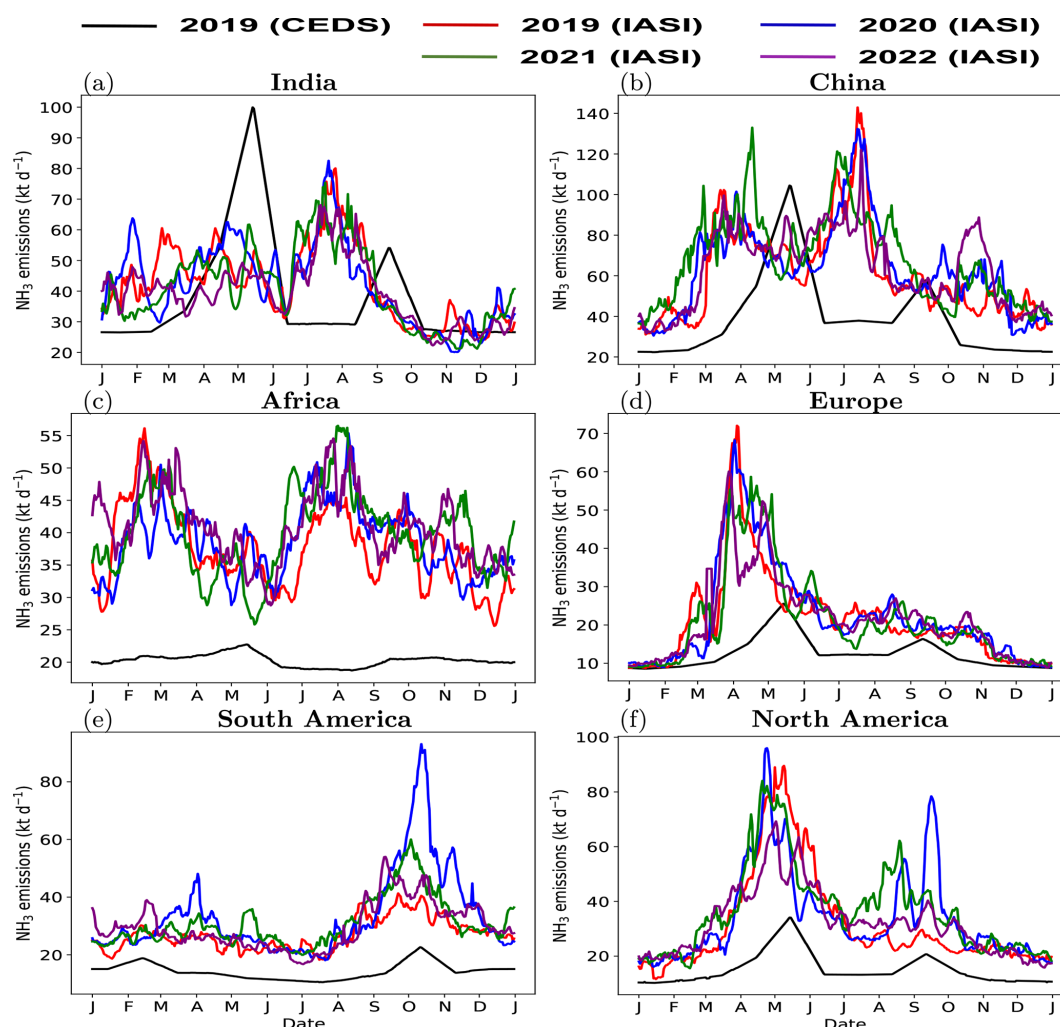


**Figure 7.** Daily (at 10 d scale) variation of the total estimated and the prior CEDS anthropogenic  $\text{NH}_3$  emissions for the 4 years from 2019 to 2022 integrated over each selected region: (a) India, (b) China, (c) Africa, (d) Europe, (e) South America, and (f) North America.

as 38 separate fires started by lightning strikes on 16–17 August 2020 in the western U.S., leading to the first “gigafire” event in modern history in California (Campbell et al., 2022; Makkaroon et al., 2023). Campbell et al. (2022) showed that this 2020 “gigafire” contributed up to 83 % of the total nitrogen emissions in the western U.S. However, based on the GFED4 inventory fire emissions, our inversion could not filter out the grids dominated by these wildfire emissions during such events in this region.

Over the European region, hotspot regions with high anthropogenic  $\text{NH}_3$  emissions are well detected from our inversion estimates (Fig. 8d). The 4-year average of the annual  $\text{NH}_3$  emission estimates over this region is estimated as  $\sim 7.9$  ( $7.7$ – $8.2$ )  $\text{Tg yr}^{-1}$  (Fig. 9d). The estimated annual emissions over this region in 2020 are higher than in the other remaining inversion years; however, the estimates still remain approximately comparable across these years (Fig. 9d). Our emission estimates over the European region are  $\sim 72$  %

higher compared to the prior CEDS anthropogenic  $\text{NH}_3$  emissions. The estimates show a strong seasonality across all years, with high emissions from March to May peaking in April (Fig. 7d). This seasonality in the estimates differs from the prior CEDS anthropogenic  $\text{NH}_3$  emissions, which show a high peak in May and a smaller one in September (Fig. 7d). The strong seasonality in the emission estimates agrees well with the crop cycle over the European region when the main cultivation activities dominate in the spring and summer seasons.

Other than these selected regions, we also briefly analyze regional estimates over the Middle East region, a comparatively smaller ammonia-emitting region (Fig. S12). A recent study by Osipov et al. (2022) based on ship-borne measurements around the Arabian Peninsula and modeling showed that  $\text{NH}_3$  emissions over the Middle East region are significantly underestimated, potentially by a factor exceeding 15, from the EDGAR inventory emission used in their model



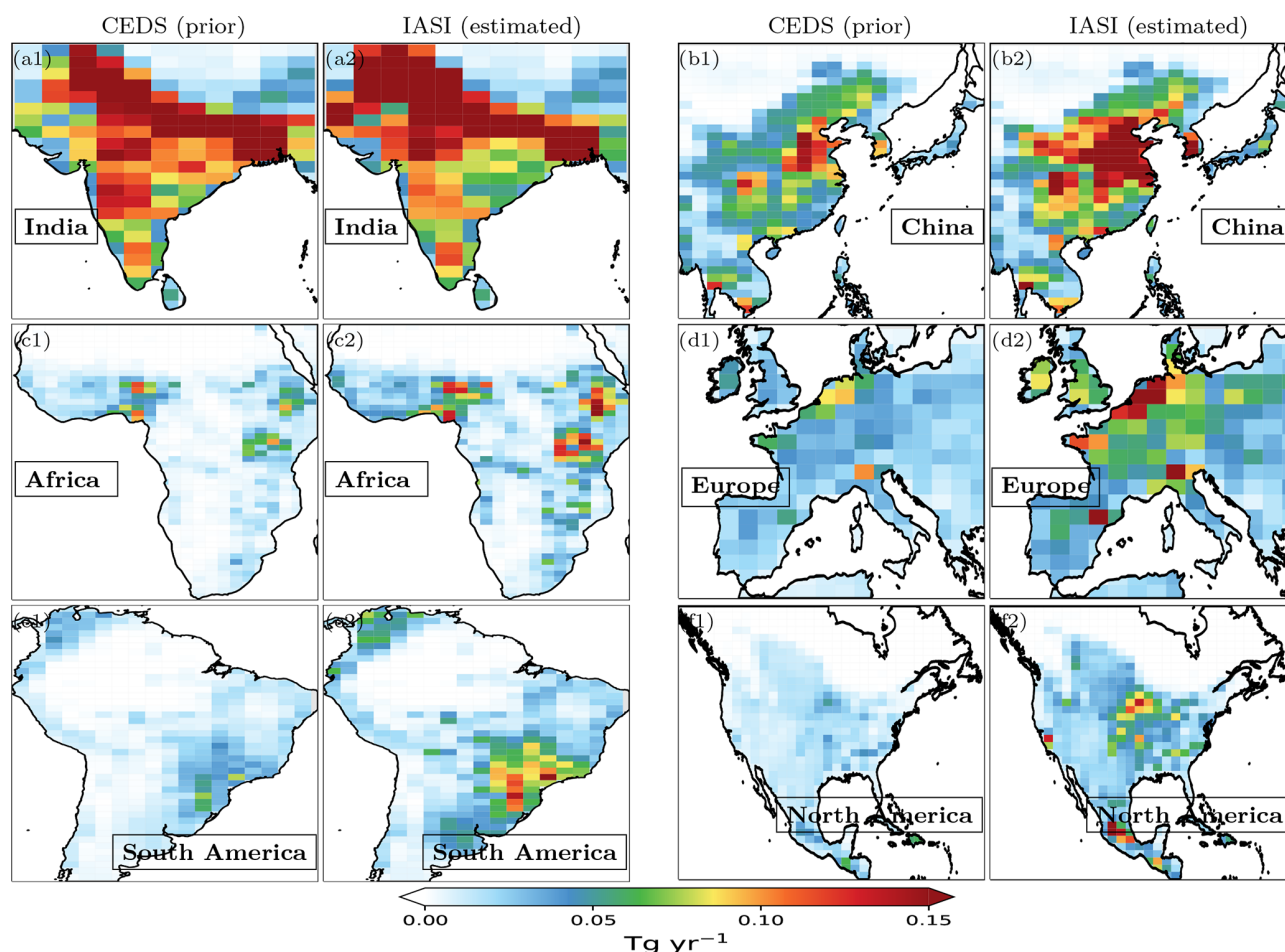


**Figure 8.** Spatial distribution of the total annual  $\text{NH}_3$  emissions averaged over the 4-year period (2019–2022) across six regions, i.e., (a) India, (b) China, (c) Africa, (d) Europe, (e) North America, and (f) South America, showing bottom-up prior CEDS emissions (first column) and IASI-constrained estimated emissions ( $E_{\text{IASI}}$ ) using the IASI  $\text{NH}_3$  observations ( $\Omega_{\text{obs}}$ ).

simulations. While natural sources of ammonia play a negligible role in this region, the vast majority of emissions arise from industrial and agricultural activities. Over the Middle East region, our average annual anthropogenic estimate of  $\sim 4.4 \text{ Tg yr}^{-1}$  ( $\sim 4.4\text{--}4.5 \text{ Tg yr}^{-1}$ ) is approximately 49 % higher than the prior CEDS emissions ( $\sim 3.0 \text{ Tg yr}^{-1}$ ). The annual  $\text{NH}_3$  emissions in these regions remained almost the same over the 4-year period (Fig. S12c). The estimated  $\text{NH}_3$  emissions show strong seasonality, with a high peak in May–April and a second peak in July–August, across all four years, whereas the prior CEDS anthropogenic  $\text{NH}_3$  emissions show two peaks: in May and in September (Fig. S12b).

## 4 Discussion

### 4.1 Comparison with bottom-up inventories and other $\text{NH}_3$ emission estimates

In this section, we compare our IASI-inverted  $\text{NH}_3$  emission estimates with other global and regional bottom-up in-

ventories, as well as with other available  $\text{NH}_3$  emission inversion estimates reported in recent literature. We use two global bottom-up  $\text{NH}_3$  emission inventories: (i) CAMS-GLOB-ANT v6.2 (developed by combining the CEDSv2 emission trends and temporal profiles from CAMS-GLOB-TEMPO and EDGAR v6 historical monthly  $\text{NH}_3$  emission data up to 2018)  $0.1^\circ \times 0.1^\circ$  monthly dataset (Granier et al., 2019; Soulie et al., 2024) from 2019 to 2022 and (ii) the process-based agricultural and natural soil  $\text{NH}_3$  emissions from the Calculation of AMmonia Emissions in ORCHIDEE (CAMEO) model at  $1.27^\circ \times 2.5^\circ$  horizontal and monthly temporal resolutions (Beaudor et al., 2023). CAMEO simulates  $\text{NH}_3$  sources from the agricultural sector, from livestock manure management (from animal housing and manure storage to grazing) to synthetic and organic nitrogen application to soil. Because CAMEO emissions are not limited only to cultivated/livestock areas and are dynamically dependent on environmental conditions and atmospheric deposition, emissions from natural ecosystems are also exploited

in this study. For these inter-comparisons, we regridded the global NH<sub>3</sub> emissions from the bottom-up inventories on the grids ( $1.27^\circ \times 2.5^\circ$ ) of our estimated emissions. We also sub-sampled the monthly emissions from the bottom-up inventories on the common grids corresponding to the IASI-constrained monthly NH<sub>3</sub> emissions derived from the daily (at 10 d scale) estimates. Note that CAMEO additionally includes natural soil NH<sub>3</sub> emissions, whereas CAMS emissions do not include them and provide only anthropogenic NH<sub>3</sub> emissions.

The 4-year (2019–2022) average of the global annual anthropogenic NH<sub>3</sub> emissions from the CAMS bottom-up inventory ( $\sim 52.5 \text{ Tg yr}^{-1}$ ), sub-sampled on the common grids where the IASI-constrained monthly emissions are available, is lower than the prior CEDS anthropogenic NH<sub>3</sub> emissions ( $\sim 60.5 \text{ Tg yr}^{-1}$ ), whereas global annual NH<sub>3</sub> emissions from CAMEO from the combined agricultural and natural soil sectors ( $\sim 71.1 \text{ Tg yr}^{-1}$ ) are higher than those from both CEDS and CAMS. Therefore, we have an even larger relative difference between the estimated and the CAMS emissions than the relative difference between the estimated and CEDS emissions (Fig. 9). However, this relative difference between the estimated and CAMEO's combined agriculture and natural soil NH<sub>3</sub> emissions is smaller compared to the relative difference between the estimated and CEDS. The 4-year-averaged global annual NH<sub>3</sub> emissions from the inversions are  $\sim 1.8$  times higher than the CAMS anthropogenic NH<sub>3</sub> emissions and  $\sim 1.4$  times higher than the CAMEO combined agriculture and natural soil NH<sub>3</sub> emissions. Figure 9 shows a comparison between the IASI-inverted annual emissions and the corresponding CAMS and CAMEO emissions over six regions (and over the Middle East in Fig. S12) and across 4 years, revealing consistently higher IASI-constrained NH<sub>3</sub> emissions compared to these global bottom-up inventories.

We also compare our estimates with the recent global NH<sub>3</sub> inversion emission estimates by Luo et al. (2022) based on a previous version of IASI NH<sub>3</sub> observations from 2008 to 2018, with the recent estimates from Dammer et al. (2022) derived using the CrIS observations from 2013 to 2020, and with some other regional inversion estimates. Luo et al. (2022) estimated global annual NH<sub>3</sub> emissions at  $\sim 78$  ( $70\text{--}92$ )  $\text{Tg yr}^{-1}$  averaged over a period from 2008 to 2018, and Dammer et al. (2022), over a period from 2013 to 2020, had  $216.6 \pm 66.2 \text{ Tg yr}^{-1}$  (for all detected source locations) and  $74.1 \pm 17.7 \text{ Tg yr}^{-1}$  (for inventory-identified source locations). Our averaged global annual NH<sub>3</sub> emission estimates of  $\sim 97$  ( $94\text{--}100$ )  $\text{Tg yr}^{-1}$  from 2019 to 2022 are  $\sim 25\%$  higher than the average total estimates ( $\sim 78 \text{ Tg yr}^{-1}$ ) from Luo et al. (2022). This can partly be explained by the fact that the IASI version 4 NH<sub>3</sub> column values used in this study are also about  $10\text{--}20\%$  higher than the earlier version 3 (Clarisse et al., 2023) used by Luo et al. (2022) due to a reduction of the retrieval biases. This also has to be explained by the use of a different inversion approach, of a

different chemistry transport model, and of AKs from IASI NH<sub>3</sub> observations to model-simulated NH<sub>3</sub> columns in this study. Our estimates align more closely with the upper range ( $\sim 92 \text{ Tg yr}^{-1}$ ) of their emission estimates obtained by setting a  $200\%$  perturbation to the modeled atmospheric NH<sub>3</sub> lifetime in their inversions. It should be noted that Luo et al. (2022) corrected their NH<sub>3</sub> emissions over the Indian and the East China regions during 2013 to 2018, which were impacted by the rapid changes in SO<sub>2</sub> emissions and concentrations in these regions, especially the rapid decrease in SO<sub>2</sub> emissions over China. A decrease in SO<sub>2</sub> emissions leads to an increase in NH<sub>3</sub> concentrations/columns in the troposphere because lower SO<sub>2</sub> levels reduce the formation of ammonium sulfate aerosols, leaving more free ammonia in the atmosphere, which increases its concentration in the air (Luo et al., 2022). This correction in Luo et al. (2022) leads to a small increase in NH<sub>3</sub> emissions over the Indian region. However, a substantial reduction of  $\sim 7\text{--}8 \text{ Tg}$  for the year 2018 is observed over the East China region. Without any correction for SO<sub>2</sub> trends, our estimates (for 2019) are closer to their estimates for the year 2018. In contrast, our average total global estimate of  $\sim 97$  ( $93.8\text{--}99.9$ )  $\text{Tg yr}^{-1}$  for the period 2019–2022 is  $\sim 2.2$  times smaller than the  $216.6 \pm 66.2 \text{ Tg yr}^{-1}$  total from the sum of all detected source estimates from Dammer et al. (2022). Additionally, our 4-year-averaged estimates are  $\sim 31\%$  higher when comparing with their estimates ( $74.1 \pm 17.7 \text{ Tg yr}^{-1}$ ) corresponding to the sources in the CAMS-GLOB-ANT v4.2 inventory emissions above the detection limit of their satellite-constrained emissions.

In order to compare our regional NH<sub>3</sub> emissions, derived from the global inversion estimates, with those of Luo et al. (2022), we regrid their final inversion year (2018) estimates to match the spatial resolution ( $1.27^\circ \times 2.5^\circ$ ) of our estimated NH<sub>3</sub> emissions. Subsequently, we integrate both the emission estimates over the identical grids on common selected regions' domains over land and compare their final inversion year's (2018) NH<sub>3</sub> emissions with our nearest first inversion year (2019) estimates. In comparison with Dammer et al. (2022), their regional estimates for all detected source locations are consistently higher than our estimates. Therefore, in the subsequent comparison analysis, we compare our estimates with only their regional reported estimates corresponding to the sources with inventory emissions above the detection limit of their satellite-derived emissions. This comparison is consistent, as our estimates also required information on the prior CEDS NH<sub>3</sub> emissions, and for the missing sources with zero emissions in the bottom-up inventory, our inversion will not detect any new emission sources. Over the Indian region, our annual estimates of 2019 ( $\sim 15.4 \text{ Tg yr}^{-1}$ ) are closer to the estimates of 2018 ( $\sim 13.1 \text{ Tg yr}^{-1}$ ) from Luo et al. (2022), representing a marginal  $\sim 18\%$  increase. Our estimates over the China region of 2019 ( $22.3 \text{ Tg yr}^{-1}$ ) are much higher ( $\sim 73\%$ ) compared to the Luo et al. (2022) SO<sub>2</sub> trend-

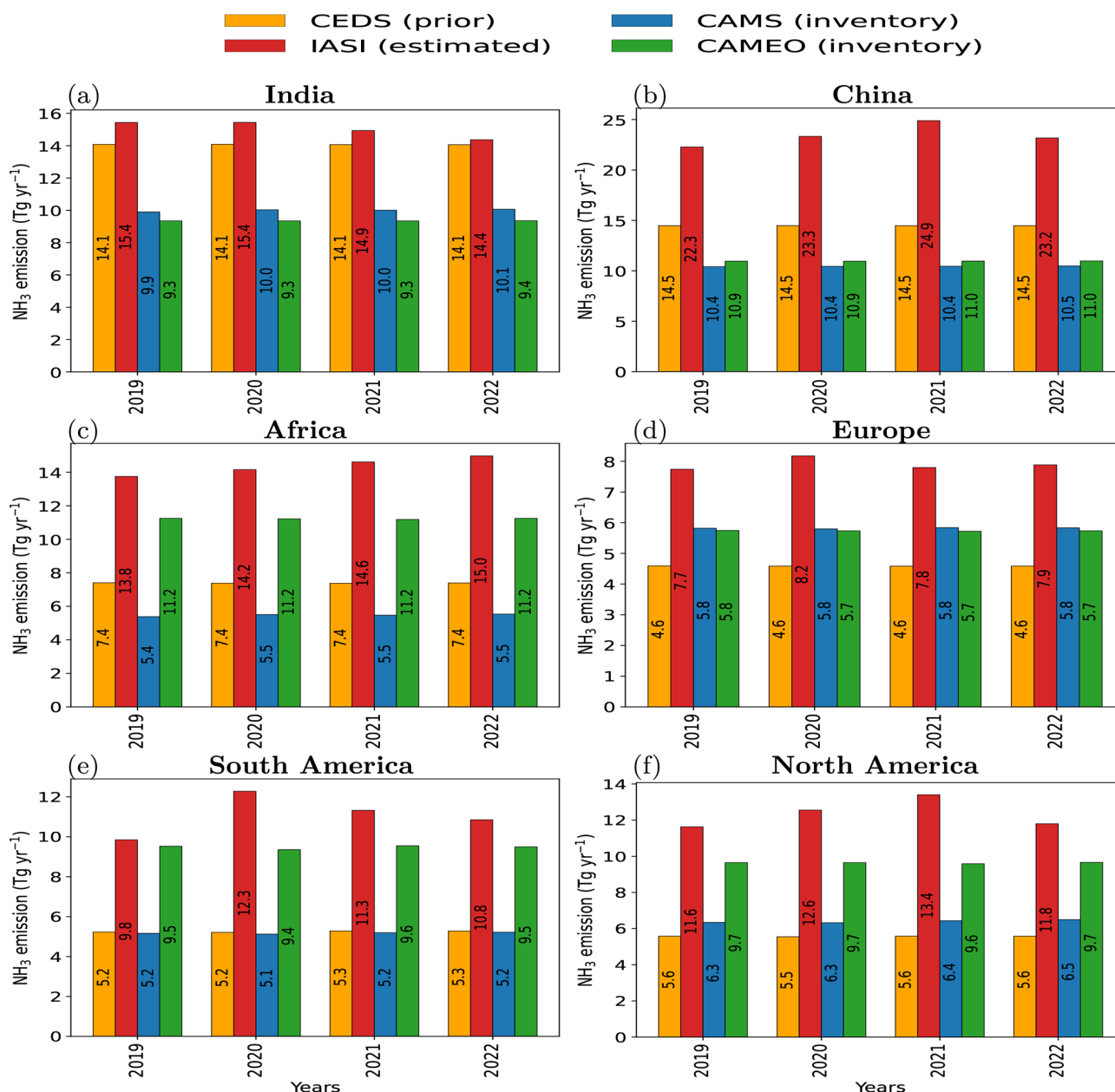


**Figure 9.** The regional annual  $\text{NH}_3$  emissions spanning from 2019 to 2022 over the six regions over land areas, derived from the IASI-constrained daily global estimates, the prior CEDS inventory anthropogenic  $\text{NH}_3$  emissions, and two independent global bottom-up inventories: CAMS (anthropogenic  $\text{NH}_3$  emissions) and CAMEO (combined agriculture and natural soil  $\text{NH}_3$  emissions). The CAMEO  $\text{NH}_3$  emissions are for the last available year, 2014, selected on the common grids of each year's estimates.

corrected  $\text{NH}_3$  emissions ( $\sim 13 \text{ Tg yr}^{-1}$ ); however, these are closer to their estimates without correction. Recently, Liu et al. (2022) estimated  $21.6 \text{ Tg NH}_3 \text{ yr}^{-1}$  ( $\equiv 17.77 \text{ Tg N yr}^{-1}$ ) annual emissions over China for the year 2019 using satellite data, and our estimates ( $22.3 \text{ Tg yr}^{-1}$ ) for the same year are comparable to these inversion estimates. Dammers et al. (2022) reported  $\sim 35 \text{ Tg yr}^{-1}$  average  $\text{NH}_3$  emissions for the Asia region, and our combined 4-year-averaged estimate of  $\sim 43 \text{ Tg yr}^{-1}$  from India, China, and the Middle East re-

gions is  $\sim 23\%$  higher than their estimate. Our estimates for Africa ( $\sim 13.8 \text{ Tg yr}^{-1}$ ), South America ( $\sim 9.8 \text{ Tg yr}^{-1}$ ), and the Middle East ( $\sim 4.4 \text{ Tg yr}^{-1}$ ) regions for 2019 agree well with the Luo et al. (2022) estimates (11.1, 10.5, and  $4.1 \text{ Tg yr}^{-1}$ , respectively) of 2018 within  $\sim 24\%$ ,  $\sim 6\%$ , and  $\sim 6\%$ , respectively. For the South American region, our annual estimate of  $\sim 9.8 \text{ Tg yr}^{-1}$  for 2019 agrees well with the estimate of  $9.1 \text{ Tg yr}^{-1}$  from Dammers et al. (2022). Our estimates ( $11.6 \text{ Tg yr}^{-1}$ ) for 2019 over the North American

region are  $\sim 55\%$  higher than  $\sim 7.5 \text{ Tg yr}^{-1}$  from Luo et al. (2022); however, they are comparable to the total estimates of  $12.2 \text{ Tg yr}^{-1}$  from Dammers et al. (2022). Recently, Sahoo et al. (2024) constructed a high-resolution gridded ( $0.1^\circ \times 0.1^\circ$ ) emission inventory of  $\text{NH}_3$  emissions over India for 2022 by including 24 regional major and minor anthropogenic sources. They estimated  $10.54 \text{ Tg yr}^{-1}$  of  $\text{NH}_3$  emissions in 2022, which are closer to the CAMS anthropogenic  $\text{NH}_3$  emissions, while our inversion estimates of  $14.4 \text{ Tg yr}^{-1}$   $\text{NH}_3$  emissions for the same year are  $\sim 36\%$  higher than their estimates (Fig. 9b). However, in this comparison analysis over the Indian region, our selected domain is larger, encompassing most of South Asia, compared to the India-only domain considered in Sahoo et al. (2024).

Over the European region, our annual  $\text{NH}_3$  estimate ( $\sim 7.7 \text{ Tg yr}^{-1}$ ) for 2019 is  $\sim 91\%$  higher compared to  $\sim 4.1 \text{ Tg yr}^{-1}$  from Luo et al. (2022) for 2018. However, our 4-year-averaged annual estimates ( $\sim 7.9 \text{ Tg yr}^{-1}$ ) are  $\sim 29\%$  smaller than  $\sim 11.1 \text{ Tg yr}^{-1}$  from the estimates of Dammers et al. (2022). The European Union (EU) emission inventory report (EEA Report No 4/2023, 2023) reported comparatively lower  $\text{NH}_3$  emissions for the EU 27 member states of 3.5, 3.4, and  $3.3 \text{ Tg yr}^{-1}$  for 2019, 2020, and 2021, respectively, which are much lower compared to our estimates for these years. Also, some other recent top-down inversion studies, such as Tichý et al. (2023), have obtained a similar order of magnitude of the emissions ( $4.3$  and  $4.0 \text{ Tg yr}^{-1}$  for 2019 and 2020, respectively) using the CrIS satellite observations from Luo et al. (2022) ( $4.1 \text{ Tg yr}^{-1}$  for 2018) or from EEA Report No 4/2023 (2023). However, our estimates are comparable to the  $\text{NH}_3$  emissions derived from a recent regional atmospheric inversion over Europe at  $0.2^\circ \times 0.2^\circ$  horizontal and monthly temporal resolutions over a 3-year period from 2020 to 2022, derived within the EU project Sentinel EO-based Emission and Deposition Service (SEEDS) (<https://www.seedsproject.eu/data/monthly-nh3-emissions>, last access: 7 August 2023) (Ding et al., 2020, 2024). In this regional atmospheric inversion,  $\text{NH}_3$  emissions over Europe were derived by the DECSO (Daily Emissions Constrained by Satellite Observations) v6.2 algorithm, developed to derive emissions of short-lived species based on an extended Kalman filter approach and using CrIS (NOAA-20) observations (Ding et al., 2020, 2024). Our annual  $\text{NH}_3$  emission estimates integrated over the common European domain [ $10^\circ \text{W}$ – $30^\circ \text{E}$ ,  $35^\circ$ – $55^\circ \text{N}$ ] of their inversions, amounting to 8.8, 8.4, and  $8.4 \text{ Tg yr}^{-1}$  for the years 2020, 2021, and 2022, respectively, are in good agreement (within  $\sim 1\%$ – $8\%$ ) with 8.2, 8.4, and  $8.6 \text{ Tg yr}^{-1}$  derived for the same years in the SEEDS  $\text{NH}_3$  emission inversions. The SEEDS  $\text{NH}_3$  emission estimates over Europe indicate an increasing trend of  $\sim 0.2 \text{ Tg yr}^{-1}$  over a 3-year period from 2020 to 2022. In contrast, our inversion estimates show a peak in 2020, with comparatively slightly lower values in the subsequent years (Fig. 9d).

This comparison analysis shows that our inversion estimates of  $\text{NH}_3$  emissions integrated at global or regional spatial scales are within the range of other previous inversion estimates derived based on different satellite observations and different inversion approaches. When comparing our IASI-based inversion estimates with some of those derived from CrIS observations, the differences in satellite overpass times (IASI  $\sim 09:30 \text{ LST}$ , CrIS  $\sim 13:30 \text{ LST}$ ) could also lead to differences in retrieved  $\text{NH}_3$  due to the potentially strong and quite uncertain diurnal variability in  $\text{NH}_3$  emissions and atmospheric concentrations and retrieval approaches. However, in the current setup of our model LMDZ-INCA, the anthropogenic  $\text{NH}_3$  emissions are derived from a 1-month-resolution inventory that is uniformly distributed in time at the hourly resolution, without incorporating diurnal cycles. This lack of diurnal variations in the input prior emissions could indeed enhance the discrepancies between IASI- and CrIS-based emission estimates. In a study by Dammers et al. (2019), they utilized both IASI and CrIS satellite observations to estimate  $\text{NH}_3$  emissions, lifetimes, and plume widths from major agricultural and industrial point sources. Their findings indicate that CrIS-derived  $\text{NH}_3$  emission estimates are, on average, slightly higher than those obtained from IASI-A and IASI-B observations. However, these differences remain within the overall uncertainty range of the estimates. The differences in the emissions from CrIS and IASI could be due to the bias between the satellite  $\text{NH}_3$  retrievals, as well as the potential influence of the different overpass times of these satellites in combination with the strong diurnal cycles of the emissions. Overall, our estimates, as well as these other inversion estimates, are higher compared to the  $\text{NH}_3$  emissions from different global or regional bottom-up inventories, which tend to support the assumption that there is a general underestimation of the emissions in the inventories. The bottom-up inventories do not accurately capture the seasonality of  $\text{NH}_3$  emissions in relation to the agricultural and crop activity cycles in some regions like India, China and the Middle East. In contrast, our inversion estimates demonstrate a seasonality that is consistent with the crops and agriculture cycles in these regions.

#### 4.2 Impact of COVID-19 lockdowns on $\text{NH}_3$ emissions

The strict restrictions imposed during the COVID-19 lockdown periods in the year 2020 across different regions/countries/cities around the world resulted in major changes in anthropogenic activities, atmospheric concentrations, and emissions of different air pollutant species like  $\text{NO}_x$  and  $\text{SO}_2$ . However, atmospheric  $\text{NH}_3$  concentration and emissions received comparatively less attention compared to  $\text{NO}_x$  or  $\text{SO}_2$ , and only a few studies analyzed the impact of COVID lockdowns on ambient  $\text{NH}_3$  concentrations. Most of the air pollutants like  $\text{NO}_x$  and  $\text{SO}_2$  show a decline in their atmospheric concentrations and emissions during the COVID-19 lockdown periods (Zheng et al., 2021). The de-



cline in NO<sub>x</sub> and SO<sub>2</sub> concentrations in the atmosphere during the COVID-19 lockdowns led to a reduction in the formation of ammonium nitrate and ammonium sulfate aerosols from atmospheric ammonia and hence a decrease in the atmospheric sink of NH<sub>3</sub>. Meanwhile, agriculture activities remained mostly unchanged during the COVID-19 lockdown periods. These factors, along with changes in meteorology and atmospheric composition, may have impacted ammonia levels in the atmosphere. A recent study by Kuttippurath et al. (2024) showed that the global atmospheric ammonia concentration increased anomalously almost everywhere around the world during the COVID-19 lockdown periods in the year 2020 compared to the previous year 2019. Some other studies at regional or city scale, e.g., Xu et al. (2022) (China), Viatte et al. (2021) (Paris, France), and Lovarelli et al. (2021) (Lombardy region in Italy), also reported an increase in ammonia concentration in the atmosphere during the COVID-19 lockdown periods in 2020. Recently, Evangeliou et al. (2025) conducted inversion estimates of NH<sub>3</sub> emissions based on satellite observations during the COVID-19 lockdowns in Europe and showed that the NH<sub>3</sub> emissions decreased by  $\sim 9.8\%$  in the first half of 2020 compared to 2016–2019. However, overall atmospheric ammonia levels increased due to reduced chemical removal from lower SO<sub>2</sub> and NO<sub>x</sub> emissions and the persistence of agricultural activity (Evangeliou et al., 2025). In this study, we analyzed the changes in estimated daily (at 10 d scale) NH<sub>3</sub> emissions from our global inversions during COVID-19 major lockdowns in 2020 compared to the estimates during the same period in pre-COVID year 2019 over six regions across the world.

From our atmospheric inversions, we observe that the annual NH<sub>3</sub> emissions worldwide and across all the selected six regions in the COVID-19 lockdowns in the year 2020 are higher compared to those in the pre-COVID year 2019 (Figs. 6 and 9). Lockdown periods varied across different regions, countries, and cities. However, following the first lockdown in China in the second-to-last week of January 2020, the majority of the first major lockdowns worldwide were implemented between March and May during that year. We defined the lockdown periods in 2020 using the most consistent common dates that aligned with the major lockdowns in each region. Figure 10 compares the estimated daily NH<sub>3</sub> emissions time series and total NH<sub>3</sub> emissions during the COVID-19 lockdown periods in 2020 with the estimated NH<sub>3</sub> emissions during the corresponding period in pre-COVID year 2019 across six regions. Daily (at 10 d scale) variation of the NH<sub>3</sub> emissions during the lockdown periods in 2020 is mostly higher compared to that in the same period in 2019 (Fig. 10). The total NH<sub>3</sub> emissions across these regions in 2020 during the lockdown periods increased by a minimum of  $\sim 5\%$  (in China) to a maximum of  $\sim 37\%$  (in South America) compared to the total emissions in this period in 2019 (Fig. 10). The total NH<sub>3</sub> emissions during the lockdown periods in 2020 compared to 2019 across India, Africa, North

America, and Europe increased by  $\sim 10\%$ ,  $\sim 6\%$ ,  $\sim 9\%$ , and  $\sim 16\%$ , respectively.

The increase in NH<sub>3</sub> emissions from our global inversions during the COVID-19 lockdown periods in 2020 across different regions, compared to the pre-COVID year 2019, raises uncertainty about whether this rise is due to an increase in NH<sub>3</sub> emission sources, due to the impact of meteorology on NH<sub>3</sub> volatilization, or due to a decrease in the atmospheric sink of NH<sub>3</sub> due to the decline in NO<sub>x</sub> and SO<sub>2</sub> emissions and concentrations during the lockdowns. However, an increase in NH<sub>3</sub> emission sources during these short lockdown periods seems unlikely, as agricultural practices, the primary source of NH<sub>3</sub> emissions, remained largely unchanged during the lockdowns. This suggests that the observed rise may be more attributable to changes in atmospheric chemistry or to the impact of meteorology on NH<sub>3</sub> volatilization and to the reduction of other species, like SO<sub>2</sub> and NO<sub>x</sub> emissions, during the lockdowns (Evangeliou et al., 2025). The single species inversion system used in this study has a limitation and a source of uncertainty to explain this rise in NH<sub>3</sub> emissions. These changes require studying the atmospheric chemistry of ammonia in response to variations in NO<sub>x</sub> and SO<sub>2</sub> levels in the atmosphere. A combined multi-species inversion of NO<sub>x</sub>, SO<sub>2</sub>, and NH<sub>3</sub> emissions would offer valuable insights into the complex chemical interactions among these air pollutant species in the atmosphere.

#### 4.3 Uncertainties and limitations of the present study

There are several uncertainties and limitations associated with our global daily (at 10 d scale) inversion of the anthropogenic NH<sub>3</sub> emissions using IASI NH<sub>3</sub> observations. Although our estimates are mostly consistent and within the range of other recent inversion emissions, our inversion approach and estimates are subject to several uncertainties and limitations. The inversion approach is directly impacted by the errors associated with the observations from the satellite NH<sub>3</sub> retrievals and from model simulations, and it does not provide the uncertainty in emission estimates. A few studies (Cooper et al., 2017; Koukouli et al., 2018) provided some information about the uncertainties in their estimates of other short-lived species like NO<sub>x</sub> or SO<sub>2</sub> using the basic or FDMB inversion approach, propagating the observation errors. Although their estimates of uncertainties do not provide the full uncertainty budget, as they do not account for uncertainties associated with model errors or the specific modeling approach, implementing a similar approach could be considered in the future to provide some indication of the uncertainties in our inversion estimates. Systematic errors in satellite retrievals, particularly notable at higher latitudes and during wintertime, may introduce inconsistencies or lead to an overestimation of emissions. Statistical inverse modeling methods (Cao et al., 2020, 2022) account for retrieval errors, but this work is generally focused on the random local and instant noise on the retrievals, and these methods are

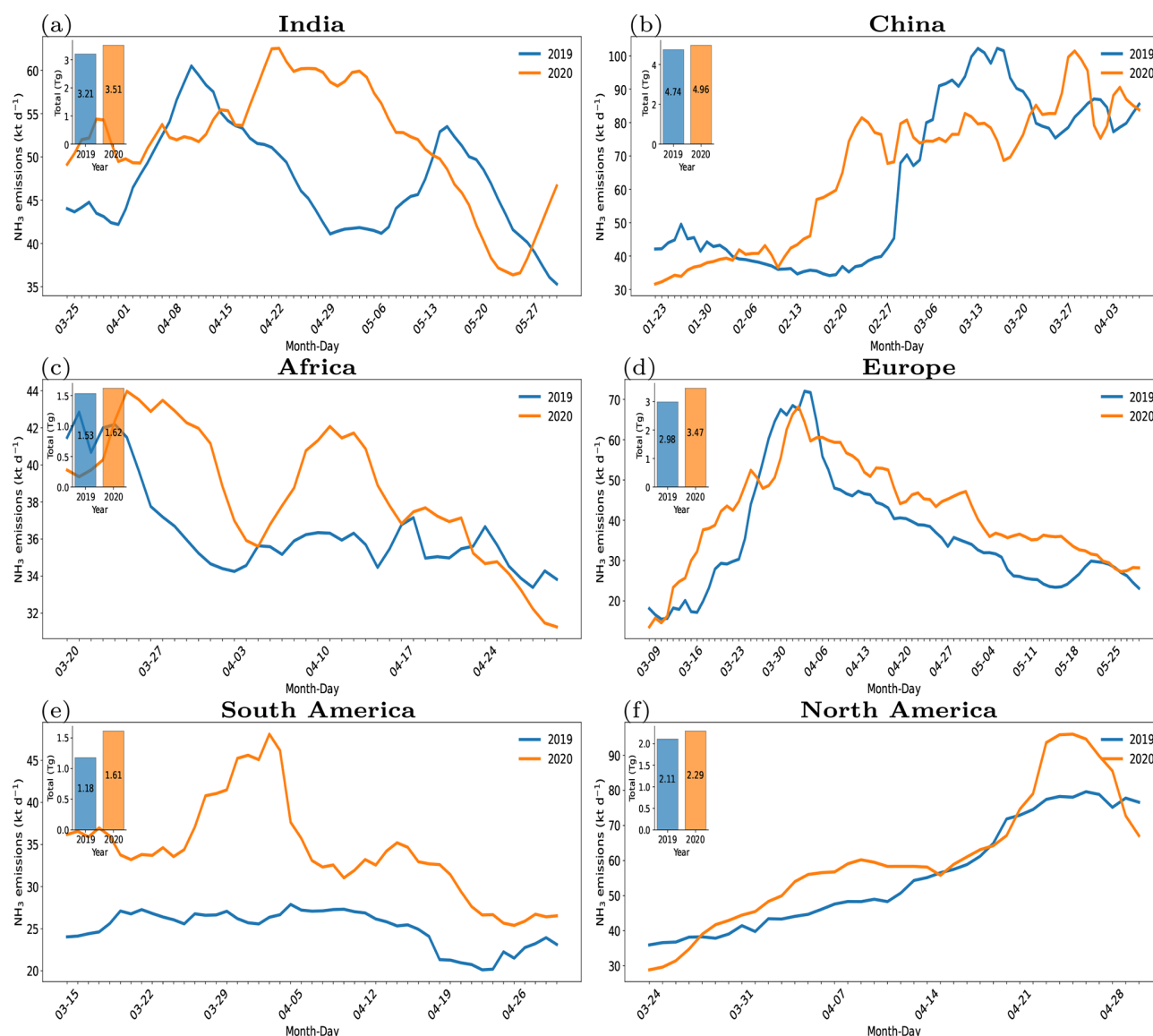


**Figure 10.** The time series of estimated daily (at 10 d scale)  $\text{NH}_3$  emissions and total emissions (bar plots) during the COVID-19 lockdown periods in the year 2020 and pre-COVID year 2019 over different regions across the world.

also highly impacted by systematic errors (Cao et al., 2020, 2022).

The FDMB inversion approach employs a linear sensitivity function based on the perturbations of  $\text{NH}_3$  emissions in LMDZ-INCA model simulations, which may oversimplify the complex chemical interactions between air pollutants, including  $\text{NH}_3$ , in the atmosphere. However, in order to test the impact on the inversion results of the selection of the level of perturbations, we have also conducted a sensitivity analysis with a LMDZ-INCA model simulation using a smaller 20 % perturbation to the prior CEDS anthropogenic  $\text{NH}_3$  emissions for the year 2019, in contrast to the original 40 % perturbation used in our FDMB inversion setup. The results show that the differences in the resulting budget of the

estimated  $\text{NH}_3$  emissions over 2019 and the globe with the application of the FDMB based on these two levels of perturbations are less than 2 %, indicating that the inversion results are not highly sensitive to the choice of perturbation magnitude within this range. As  $\beta$  is the only variable that changes when changing the level of perturbation, this less than 2 % change in the emission estimates necessarily stems from the changes in  $\beta$  due to the reduced prior  $\text{NH}_3$  emission perturbations. The good fit between the model simulations with the inverted  $\text{NH}_3$  emissions and the IASI  $\text{NH}_3$  observations (Sect. 3.2) further strengthens the confidence in the linearization of the inversion problem based on 40 % perturbations to the prior estimate of the emissions. This sensitivity behavior is similar to that of previous applications of the FDMB

method to the inversions of anthropogenic  $\text{NO}_x$  emissions, where different perturbation levels (e.g., 5 %–50 %) to the prior emissions resulted in minimal changes in the posterior anthropogenic  $\text{NO}_x$  emission estimates at global and regional scales (Cooper et al., 2017; Lamsal et al., 2011; Zheng et al., 2020). The use of a 40 % perturbation in our  $\text{NH}_3$  study was motivated by the relatively high uncertainty in the current  $\text{NH}_3$  emission inventories, particularly over regions with strong agricultural sources. Nevertheless, our sensitivity test indicates that this choice (at least within a range of 20 %–40 %) is not a critical parameter of our inversions.

Due to the sparseness of daily satellite observations of  $\text{NH}_3$  total columns, when the number of high-quality observations within a grid cell is limited, it amplifies uncertainty in the averaged gridded dataset used in the inversions. Consequently, this may lead to an increase in uncertainty in the estimates of daily (at 10 d scale) emissions. As we focus on the inversion of dominated anthropogenic  $\text{NH}_3$  emissions, exclusion of the emissions from other sectors like natural sources is a big challenge. This complexity is particularly pronounced in regions dominated by biomass burning  $\text{NH}_3$  emissions from wildfires. The local mass-balance inversion approach does not incorporate the transport of ammonia from the non-local biomass burning emissions regions to the local anthropogenic grids, which may lead to an overestimation of the anthropogenic  $\text{NH}_3$  emissions in some regions like South America, North America, and Africa. Furthermore, the conservative gap-filling approach employed in this study may introduce some biases and contribute to uncertainties in the final emission estimates.

Although the local finite difference mass-balance approach applied for the inversion of short-lived species like  $\text{NH}_3$  in this study, which has a typical short atmospheric lifetime of a few hours to a day, is suitable for inversions at a coarse resolution ( $\sim 2^\circ$ ) (Cooper et al., 2017), the typical length scale of our model's spatial resolution ( $1.27^\circ \times 2.5^\circ$ ) can often be reached by the advection of  $\text{NH}_3$  within its lifetime. The transport to neighboring grids can lead to a spatial “smearing” effect, where emissions are dispersed away from their source grid cell, introducing errors in mass-balance inversion approaches (Cooper et al., 2017; Li et al., 2019). This problem of spatial smearing in mass-balance inversion approaches is well-documented for short-lived species like  $\text{NO}_x$  or  $\text{NH}_3$  (Cooper et al., 2017; Li et al., 2019). Such smearing can lead, on average, to the underestimation of the regional-scale emissions, as the approach overlooks the fact that the amplitude of the  $\text{NH}_3$  signal associated with a given area source decreases with the advection downwind (Cooper et al., 2017; Li et al., 2019). For short-lived species like  $\text{NO}_x$ , some approaches such as smoothing kernels or iterative FDMB inversion approaches have been used to reduce these errors, but the latter is computationally intensive, especially for global inversions. An iterative FDMB approach (Cooper et al., 2017; Li et al., 2019) can be explored in the future to

provide better accuracy in the estimates of  $\text{NH}_3$  emissions at a feasible computational cost to overcome this limitation.

In our LMDZ-INCA model setup and inversion framework, the CEDS inventory emissions are regridded to match the model resolution. While this inevitably misses some fine-scale features, our study focuses on the broader regional patterns of  $\text{NH}_3$  emissions rather than point-source inversions. The inversions at higher resolution, based on high-resolution regional inventories (e.g., MEIC, NEI, and CAMS-REG) and high-resolution chemistry transport model simulations can bring more robust information of the more localized  $\text{NH}_3$  sources such as point sources at sub-national scales. However, the above-mentioned limitation, i.e., the spatial smearing effect (ignoring the advection across the chemistry transport model grid cells) of the FDMB inversion approach, would be exacerbated at such a higher resolution. Even if an iterative FDMB approach is used to overcome this smearing effect at finer resolutions, errors in the derived emission estimates can be amplified (Li et al., 2019). Therefore, application of such an inversion approach at the finer resolution may have limitations in accurately estimating the  $\text{NH}_3$  emissions.

Note that an inverse modeling framework including observations of the full reduced nitrogen family ( $\text{NH}_x = \text{NH}_3 + \text{NH}_4^+$ ) and relying on tests of sensitivities of  $\text{NH}_3$  and  $\text{NH}_4^+$  to changes in  $\text{NH}_3$  emissions could provide a more comprehensive constraint on  $\text{NH}_3$  emissions, given the rapid gas-particle partitioning of  $\text{NH}_3$  to  $\text{NH}_4^+$  under typical atmospheric conditions. However, current satellite retrievals such as those from IASI and CrIS are primarily focused on gaseous  $\text{NH}_3$ . The current spaceborne instruments have a limited capability to detect particulate-phase  $\text{NH}_4^+$ . As a result, the observational constraints in our inversion framework are based only on  $\text{NH}_3$  columns. Nevertheless, the LMDZ-INCA aerosols–chemistry transport model used in our inversion framework fully represents these chemical conversions of  $\text{NH}_3$  to  $\text{NH}_4^+$  and the partitioning and deposition processes affecting the entire  $\text{NH}_x$  family. Therefore, the LMDZ-INCA model and, implicitly, our inversion framework account for the fate of  $\text{NH}_3$  through its interaction with  $\text{NH}_4^+$  when deriving relationships between the  $\text{NH}_3$  emissions and concentrations.

Over some regions like China and India, the rapid changes in  $\text{SO}_2$  emissions in recent years impact the  $\text{NH}_3$  concentration in the atmosphere significantly and thus emissions (Luo et al., 2022). Similarly, changes in  $\text{NO}_x$  emissions and concentration in the atmosphere across different regions alter the formation of ammonium nitrate from ambient ammonia. Therefore, we will investigate the potential of simultaneously assimilating  $\text{NH}_3$ ,  $\text{SO}_2$ , and  $\text{NO}_x$  satellite observations to constrain the  $\text{NH}_3$  emissions in future studies.

## 5 Conclusions

In this study, we present satellite-based atmospheric inversion estimates of the global daily (at 10 d scale) NH<sub>3</sub> emissions for a period of 4 years from 2019 to 2022 at  $1.27^{\circ} \times 2.5^{\circ}$  horizontal resolution using the new version 4 of the IASI-ANNI-NH<sub>3</sub>-v4 NH<sub>3</sub> observations and the LMDZ-INCA model simulations. We take advantage of the averaging kernel provided in the IASI-ANNI-NH<sub>3</sub>-v4 data product to evaluate the LMDZ-INCA model suitability for global inversion of the NH<sub>3</sub> emissions. The LMDZ-INCA model-simulated NH<sub>3</sub> total columns using the prior NH<sub>3</sub> emissions are underestimated from the IASI NH<sub>3</sub> observations over most of the selected regions, except over the Indian region, and over a region in Eastern Siberia, where the model shows an overall overestimation from the observations. The simulated NH<sub>3</sub> columns from the LMDZ-INCA model followed the seasonality of the IASI observations over the South American and North American regions and, to some extent, over the European region. However, the seasonal variations over the Indian, Chinese, and African regions are inadequately represented in the model simulations compared to the IASI NH<sub>3</sub> observations.

We use a simple finite difference mass-balance approach for the inversion of global daily (at 10 d scale) NH<sub>3</sub> emissions using the LMDZ-INCA and IASI NH<sub>3</sub> total NH<sub>3</sub> columns that uses a sensitivity parameter of NH<sub>3</sub> columns to changes in the local NH<sub>3</sub> emissions to address non-linear chemistry effects from the model simulations. By conducting an evaluation simulation with the LMDZ-INCA model using IASI-constrained NH<sub>3</sub> emission estimates derived from our global atmospheric inversions for the year 2019, we demonstrate that the substantial improvements in model agreement with the IASI NH<sub>3</sub> observations compared to those using prior NH<sub>3</sub> emissions, across different spatiotemporal scales, strongly validate the robustness and internal consistency of our inversion framework, despite its simplified linearization approach. Our inversions provided an average of  $\sim 97$  ( $\sim 94$ – $100$ ) Tg yr<sup>-1</sup> global annual NH<sub>3</sub> emissions over a period of 4 years from 2019 to 2022. Our IASI-constrained NH<sub>3</sub> emission estimates are  $\sim 61\%$  ( $\sim 55\%$ – $65\%$ ) higher than the prior CEDS anthropogenic NH<sub>3</sub> emissions used in the inversions. A comparison of our inversion estimates with the two independent global bottom-up inventories CAMS and CAMEO shows that our estimates are  $\sim 1.8$  times higher than the CAMS anthropogenic NH<sub>3</sub> emissions and  $\sim 1.4$  times higher than CAMEO's combined agricultural and natural soil NH<sub>3</sub> emissions. Our global and regional NH<sub>3</sub> emission estimates over India, China, Africa, Europe, South America, North America, and the Middle East are mostly within the range of other global and regional inversion estimates derived based on the IASI or CrIS satellite NH<sub>3</sub> observations. Our simple inversion framework lacks the ability to attribute contributions from the sectors like biomass burning to the estimates of the anthropogenic NH<sub>3</sub> emissions.

Therefore, the estimated NH<sub>3</sub> emissions over some regions like South America and Africa may be overestimated due to predominant biomass burning from wildfires in these regions. Our NH<sub>3</sub> emission estimates over Europe are  $\sim 72\%$  higher compared to the prior CEDS inventory emissions; however, they are consistent with two recent inversion estimates. We observed an increasing trend of the NH<sub>3</sub> emission over China and Africa and a decreasing trend over the Indian region over a 4-year period from 2019 to 2022. Our estimates of the NH<sub>3</sub> emissions show a strong seasonal variation over most of the selected regions that is currently poorly known or almost absent in bottom-up inventories.

We also analyzed the impact of restrictions during the COVID-19 lockdown periods in 2020 over different regions across the world on the estimated daily (at 10 d scale) NH<sub>3</sub> emissions in comparison to the pre-COVID year 2019. Our inversion estimates show that the total NH<sub>3</sub> emissions across China, India, Africa, North America, Europe, and South America during the lockdown periods in the year 2020 increased by, respectively,  $\sim 5\%$ ,  $\sim 10\%$ ,  $\sim 6\%$ ,  $\sim 9\%$ ,  $\sim 16\%$ , and  $\sim 37\%$  compared to the total emissions in the same periods in 2019. However, this increase in NH<sub>3</sub> emissions from our global atmospheric inversions during the COVID-19 lockdowns, compared to the pre-COVID year 2019, raises a question about whether this rise is due to an increase in NH<sub>3</sub> emission sources, due to the impact of meteorology on NH<sub>3</sub> volatilization, or due to a decrease in the atmospheric sink of atmospheric NH<sub>3</sub> due to the decline in NO<sub>x</sub> and SO<sub>2</sub> emissions and ambient concentrations during the lockdown periods. However, our inversion system fails to explain this rise in NH<sub>3</sub> emissions. Therefore, a more comprehensive inversion approach, integrating NO<sub>x</sub>, SO<sub>2</sub>, and NH<sub>3</sub> simultaneously, would provide deeper insights into the complex chemical interactions between these pollutants in the atmosphere.

**Code and data availability.** All the estimated emission datasets are available from the ESA World Emission (WOREM) project website (<https://app.world-emission.com/detail/global/nh3/nh3>, last access: 17 July 2025). The IASI-ANNI-NH<sub>3</sub> version 4 dataset is available from the AERIS data infrastructure <https://iasi.aeris-data.fr/nh3/> (IASI, 2025). CAMS anthropogenic emissions CAMS-GLOB-ANT\_v5.3 data can be accessed directly from <https://doi.org/10.24380/eets-qd81> (Soulie et al., 2023). The NH<sub>3</sub> emission estimates from the Luo et al. (2022) dataset for the year 2018, used for the comparison analysis, are available from GitHub: <https://github.com/bnulzq/NH3-emission.git> (last access: 16 September 2023). The codes and scripts developed for inversions, plotting, and other analysis are accessible upon reasonable request from the corresponding author. The LMDZ-INCA global model is part of the Institut Pierre Simon Laplace (IPSL) climate modeling center's coupled model. Documentation and source code are available here: <https://cmc.ipsl.fr/ipslclimate-models/ipsl-cm6/> (last access: 7 October 2025).



**Supplement.** The supplement related to this article is available online at <https://doi.org/10.5194/acp-25-12379-2025-supplement>.

**Author contributions.** PK: Conceptualization, computations, code development, data curation, formal analysis, investigation, methodology, validation, visualization, writing (original draft), review and editing. GB, DH, PCi: Conceptualization, supervision, methodology, investigation, funding acquisition, project administration, writing, review and editing. MB: CAMEO inventory NH<sub>3</sub> emission dataset, review and editing. LC, MVD, PCo: IASI version 4 NH<sub>3</sub> dataset, review and editing. AC: LMDZ-INCA model, review and editing. BZ: CEDS inventory emission dataset, review and editing. BRR: Project administration, funding acquisition, review and editing. AD: Project administration, funding acquisition, review and editing.

**Competing interests.** The contact author has declared that none of the authors has any competing interests.

**Disclaimer.** Publisher's note: Copernicus Publications remains neutral with regard to jurisdictional claims made in the text, published maps, institutional affiliations, or any other geographical representation in this paper. While Copernicus Publications makes every effort to include appropriate place names, the final responsibility lies with the authors.

**Acknowledgements.** We extend our gratitude to all the data providers, whose contributions were essential to this study. We wish to thank Julien Bruna (LSCE) and his team for their computer support. This study was conducted in the frame of the World Emission project funded by the European Space Agency (ESA).

**Financial support.** This study received funding from the European Space Agency WORld EMISSION (WOREM) project (<https://www.world-emission.com>, last access: 15 July 2025) (ESA Contract No. 4000137291/22/I-EF). Didier Hauglustaine also acknowledges the support from the Research Council of Norway under project no. 336227 “AMMONIA: Climate and environmental impacts of green ammonia (NH<sub>3</sub>)”. The simulations were performed using HPC resources from GENCI (Grand Equipement National de Calcul Intensif) under project gen2201. Lieven Clarisse is a Senior Research Associate supported by the Belgian F.R.S.-FNRS. Martin Van Damme is supported by the FED-tWIN project ARENBERG (“Assessing the Reactive Nitrogen Budget and Emissions at Regional and Global Scales”) funded via the Belgian Science Policy Office (BELSPO).

**Review statement.** This paper was edited by Jayanarayanan Kutippurath and reviewed by three anonymous referees.

## References

- Beale, C. A., Paulot, F., Randles, C. A., Wang, R., Guo, X., Clarisse, L., Van Damme, M., Coheur, P. F., Clerbaux, C., Shephard, M. W., Dammers, E., Cady-Pereira, K., and Zondlo, M. A.: Large sub-regional differences of ammonia seasonal patterns over India reveal inventory discrepancies, *Environ. Res. Lett.*, 17, 104006, <https://doi.org/10.1088/1748-9326/AC881F>, 2022.
- Beaudor, M., Vuichard, N., Lathi  re, J., Evangeliou, N., Van Damme, M., Clarisse, L., and Hauglustaine, D.: Global agricultural ammonia emissions simulated with the ORCHIDEE land surface model, *Geosci. Model Dev.*, 16, 1053–1081, <https://doi.org/10.5194/gmd-16-1053-2023>, 2023.
- Beaudor, M., Vuichard, N., Lathi  re, J., and Hauglustaine, D.: Future trends of global agricultural emissions of ammonia in a changing climate, *Journal of Advances in Modeling Earth Systems*, 17, e2023MS004186, <https://doi.org/10.1029/2023MS004186>, 2025.
- Beer, R., Shephard, M. W., Kulawik, S. S., Clough, S. A., Eldering, A., Bowman, K. W., Sander, S. P., Fisher, B. M., Payne, V. H., Luo, M., Osterman, G. B., and Worden, J. R.: First satellite observations of lower tropospheric ammonia and methanol, *Geophys. Res. Lett.*, 35, L09801, <https://doi.org/10.1029/2008GL033642>, 2008.
- Behera, S. N., Sharma, M., Aneja, V. P., and Balasubramanian, R.: Ammonia in the atmosphere: A review on emission sources, atmospheric chemistry and deposition on terrestrial bodies, *Environ. Sci. Pollut. Res.*, 20, 8092–8131, <https://doi.org/10.1007/S11356-013-2051-9>, 2013.
- Boersma, K. F., Eskes, H. J., and Brinksma, E. J.: Error analysis for tropospheric NO<sub>2</sub> retrieval from space, *J. Geophys. Res.-Atmos.*, 109, 4311, <https://doi.org/10.1029/2003JD003962>, 2004.
- Boucher, O., Servonnat, J., Albright, A. L., Aumont, O., Balkanski, Y., Bastrikov, V., Bekki, S., Bonnet, R., Bony, S., Bopp, L., Braconnot, P., Brockmann, P., Cadule, P., Caubel, A., Cheruy, F., Codron, F., Cozic, A., Cugnet, D., D’Andrea, F., Davini, P., de Lavergne, C., Denvil, S., Deshayes, J., Devilliers, M., Ducharne, A., Dufresne, J. L., Dupont, E.,   th  , C., Fairhead, L., Falletti, L., Flavoni, S., Foujols, M. A., Gardoll, S., Gastineau, G., Ghattas, J., Grandpeix, J. Y., Guenet, B., Guez, L. E., Guilyardi, E., Guimberteau, M., Hauglustaine, D., Hourdin, F., Idelkadi, A., Joussaume, S., Kageyama, M., Khodri, M., Krinner, G., Lebas, N., Levvasseur, G., L  vy, C., Li, L., Lott, F., Lurton, T., Luyssaert, S., Madec, G., Madeleine, J. B., Maignan, F., Marchand, M., Marti, O., Mellul, L., Meurdesoif, Y., Mignot, J., Musat, I., Ottl  , C., Peylin, P., Planton, Y., Polcher, J., Rio, C., Rochetin, N., Rousset, C., Sepulchre, P., Sima, A., Swingedouw, D., Thi  blemont, R., Traore, A. K., Vancoppenolle, M., Vial, J., Vialard, J., Viovy, N., and Vuichard, N.: Presentation and Evaluation of the IPSL-CM6A-LR Climate Model, *J. Adv. Model. Earth Sy.*, 12, e2019MS002010, <https://doi.org/10.1029/2019MS002010>, 2020.
- Bouwman, A. F., Lee, D. S., Asman, W. A. H., Dentener, F. J., Van Der Hoek, K. W., and Olivier, J. G. J.: A global high-resolution emission inventory for ammonia, *Global Biogeochem. Cycles*, 11, 561–587, <https://doi.org/10.1029/97GB02266>, 1997.
- Cady-Pereira, K. E., Guo, X., Wang, R., Leytem, A. B., Calkins, C., Berry, E., Sun, K., M  ller, M., Wisthaler, A., Payne, V. H., Shephard, M. W., Zondlo, M. A., and Kantechev, V.: Validation

- of MUSES NH<sub>3</sub> observations from AIRS and CrIS against aircraft measurements from DISCOVER-AQ and a surface network in the Magic Valley, *Atmos. Meas. Tech.*, 17, 15–36, <https://doi.org/10.5194/amt-17-15-2024>, 2024.
- Campbell, P. C., Tong, D., Saylor, R., Li, Y., Ma, S., Zhang, X., Kondragunta, S., and Li, F.: Pronounced increases in nitrogen emissions and deposition due to the historic 2020 wildfires in the western U.S., *Sci. Total Environ.*, 839, 156130, <https://doi.org/10.1016/J.SCITOTENV.2022.156130>, 2022.
- Cao, H., Henze, D. K., Shephard, M. W., Dammers, E., Cady-Pereira, K., Alvarado, M., Lonsdale, C., Luo, G., Yu, F., Zhu, L., Danielson, C. G., and Edgerton, E. S.: Inverse modeling of NH<sub>3</sub> sources using CrIS remote sensing measurements, *Environ. Res. Lett.*, 15, 104082, <https://doi.org/10.1088/1748-9326/ABB5CC>, 2020.
- Cao, H., Henze, D. K., Zhu, L., Shephard, M. W., Cady-Pereira, K., Dammers, E., Sitwell, M., Heath, N., Lonsdale, C., Bash, J. O., Miyazaki, K., Flechard, C., Fauvel, Y., Kruit, R. W., Feigenspan, S., Brümmer, C., Schrader, F., Twigg, M. M., Leeson, S., Tang, Y. S., Stephens, A. C. M., Braban, C., Vincent, K., Meier, M., Seidler, E., Geels, C., Ellermann, T., Sanocka, A., and Capps, S. L.: 4D-Var Inversion of European NH<sub>3</sub> Emissions Using CrIS NH<sub>3</sub> Measurements and GEOS-Chem Adjoint With Bi-Directional and Uni-Directional Flux Schemes, *J. Geophys. Res.-Atmos.*, 127, e2021JD035687, <https://doi.org/10.1029/2021JD035687>, 2022.
- Chen, J., Cheng, M., Krol, M., de Vries, W., Zhu, Q., Liu, X., Zhang, F., and Xu, W.: Trends in anthropogenic ammonia emissions in China since 1980: A review of approaches and estimations, *Front. Environ. Sci.*, 11, 1133753, <https://doi.org/10.3389/FENVS.2023.1133753>, 2023a.
- Chen, Y., Shen, H., Kaiser, J., Hu, Y., Capps, S. L., Zhao, S., Hakami, A., Shih, J.-S., Pavur, G. K., Turner, M. D., Henze, D. K., Resler, J., Nenes, A., Napelenok, S. L., Bash, J. O., Fahey, K. M., Carmichael, G. R., Chai, T., Clarisse, L., Coheur, P.-F., Van Damme, M., and Russell, A. G.: High-resolution hybrid inversion of IASI ammonia columns to constrain US ammonia emissions using the CMAQ adjoint model, *Atmos. Chem. Phys.*, 21, 2067–2082, <https://doi.org/10.5194/acp-21-2067-2021>, 2021.
- Chen, Y., Hall, J., van Wees, D., Andela, N., Hantson, S., Giglio, L., van der Werf, G. R., Morton, D. C., and Randerson, J. T.: Multi-decadal trends and variability in burned area from the fifth version of the Global Fire Emissions Database (GFED5), *Earth Syst. Sci. Data*, 15, 5227–5259, <https://doi.org/10.5194/essd-15-5227-2023>, 2023b.
- Clarisse, L., Clerbaux, C., Dentener, F., Hurtmans, D., and Coheur, P. F.: Global ammonia distribution derived from infrared satellite observations, *Nat. Geosci.*, 2, 479–483, <https://doi.org/10.1038/NGEO551>, 2009.
- Clarisse, L., Shephard, M. W., Dentener, F., Hurtmans, D., Cady-Pereira, K., Karagulian, F., Van Damme, M., Clerbaux, C., and Coheur, P. F.: Satellite monitoring of ammonia: A case study of the San Joaquin Valley, *J. Geophys. Res.-Atmos.*, 115, 13302, <https://doi.org/10.1029/2009JD013291>, 2010.
- Clarisse, L., Franco, B., Van Damme, M., Di Gioacchino, T., Hadji-Lazaro, J., Whitburn, S., Noppen, L., Hurtmans, D., Clerbaux, C., and Coheur, P.: The IASI NH<sub>3</sub> version 4 product: averaging kernels and improved consistency, *Atmos. Meas. Tech.*, 16, 5009–5028, <https://doi.org/10.5194/amt-16-5009-2023>, 2023.
- Clerbaux, C., Boynard, A., Clarisse, L., George, M., Hadji-Lazaro, J., Herbin, H., Hurtmans, D., Pommier, M., Razavi, A., Turquety, S., Wespes, C., and Coheur, P.-F.: Monitoring of atmospheric composition using the thermal infrared IASI/MetOp sounder, *Atmos. Chem. Phys.*, 9, 6041–6054, <https://doi.org/10.5194/acp-9-6041-2009>, 2009.
- Cooper, M., Martin, R. V., Padmanabhan, A., and Henze, D. K.: Comparing mass balance and adjoint methods for inverse modeling of nitrogen dioxide columns for global nitrogen oxide emissions, *J. Geophys. Res.-Atmos.*, 122, 4718–4734, <https://doi.org/10.1002/2016JD025985>, 2017.
- Cooper, M. J., Martin, R. V., Henze, D. K., and Jones, D. B. A.: Effects of a priori profile shape assumptions on comparisons between satellite NO<sub>2</sub> columns and model simulations, *Atmos. Chem. Phys.*, 20, 7231–7241, <https://doi.org/10.5194/acp-20-7231-2020>, 2020.
- Crippa, M., Guizzardi, D., Muntean, M., Schaaf, E., Dentener, F., van Aardenne, J. A., Monni, S., Doering, U., Olivier, J. G. J., Pagliari, V., and Janssens-Maenhout, G.: Gridded emissions of air pollutants for the period 1970–2012 within EDGAR v4.3.2, *Earth Syst. Sci. Data*, 10, 1987–2013, <https://doi.org/10.5194/essd-10-1987-2018>, 2018.
- Dammers, E., McLinden, C. A., Griffin, D., Shephard, M. W., van der Graaf, S., Lutsch, E., Schaap, M., Gainairu-Matz, Y., Fioletov, V., Van Damme, M., Whitburn, S., Clarisse, L., Cady-Pereira, K., Clerbaux, C., Coheur, P. F., and Erisman, J. W.: NH<sub>3</sub> emissions from large point sources derived from CrIS and IASI satellite observations, *Atmos. Chem. Phys.*, 19, 12261–12293, <https://doi.org/10.5194/acp-19-12261-2019>, 2019.
- Dammers, E., Shephard, M., Chow, E., White, E., Hickman, J., Tokaya, J., Lutsch, E., Kharol, S., van der Graaf, S., Cady-Pereira, K., Bittman, S., McLinden, C., Erisman, J. W., and Schaap, M.: County-level ammonia emissions monitored worldwide, *Research Square* [preprint], <https://doi.org/10.21203/RS.3.RS-1752718/V1>, 2022.
- Di Gioacchino, T., Clarisse, L., Noppen, L., Van Damme, M., Bauduin, S., and Coheur, P.: Spatial and Temporal Variations of Thermal Contrast in the Planetary Boundary Layer, *J. Remote Sens. (United States)*, 28, <https://doi.org/10.34133/REMOTESENSING.0142>, 2024.
- Ding, J., van der A, R. J., Eskes, H. J., Mijling, B., Stavrou, T., van Geffen, J. H. G. M., and Veefkind, J. P.: NO<sub>x</sub> Emissions Reduction and Rebound in China Due to the COVID-19 Crisis, *Geophys. Res. Lett.*, 47, e2020GL089912, <https://doi.org/10.1029/2020GL089912>, 2020.
- Ding, J., van der A, R., Eskes, H., Dammers, E., Shephard, M., Wichink Kruit, R., Guevara, M., and Tarrason, L.: Ammonia emission estimates using CrIS satellite observations over Europe, *Atmos. Chem. Phys.*, 24, 10583–10599, <https://doi.org/10.5194/acp-24-10583-2024>, 2024.
- Douros, J., Eskes, H., van Geffen, J., Boersma, K. F., Compornolle, S., Pinardi, G., Blechschmidt, A.-M., Peuch, V.-H., Colette, A., and Veefkind, P.: Comparing Sentinel-5P TROPOMI NO<sub>2</sub> column observations with the CAMS regional air quality ensemble, *Geosci. Model Dev.*, 16, 509–534, <https://doi.org/10.5194/gmd-16-509-2023>, 2023.

- EEA Report No 4/2023: European Union emission inventory report 1990–2021 – European Environment Agency, <https://doi.org/10.2800/68478>, 2023.
- Emanuel, K. A.: A Scheme for Representing Cumulus Convection in Large-Scale Models, *J. Atmos. Sci.*, 48, 2313–2329, [https://doi.org/10.1175/1520-0469\(1991\)048<2313:ASFRCC>2.0.CO;2](https://doi.org/10.1175/1520-0469(1991)048<2313:ASFRCC>2.0.CO;2), 1991.
- Eskes, H. J. and Boersma, K. F.: Averaging kernels for DOAS total-column satellite retrievals, *Atmos. Chem. Phys.*, 3, 1285–1291, <https://doi.org/10.5194/acp-3-1285-2003>, 2003.
- Evangelou, N., Balkanski, Y., Eckhardt, S., Cozic, A., Van Damme, M., Coheur, P.-F., Clarisse, L., Shephard, M. W., Cady-Pereira, K. E., and Hauglustaine, D.: 10-year satellite-constrained fluxes of ammonia improve performance of chemistry transport models, *Atmos. Chem. Phys.*, 21, 4431–4451, <https://doi.org/10.5194/acp-21-4431-2021>, 2021.
- Evangelou, N., Tichý, O., Svendby Otervik, M., Eckhardt, S., Balkanski, Y., and Hauglustaine, D. A.: Unchanged PM<sub>2.5</sub> levels over Europe during COVID-19 were buffered by ammonia, *Aerosol Research*, 3, 155–174, <https://doi.org/10.5194/ar-3-155-2025>, 2025.
- Fortems-Cheiney, A., Dufour, G., Dufossé, K., Couvidat, F., Gilliot, J.-M., Siour, G., Beekmann, M., Foret, G., Meleux, F., Clarisse, L., Coheur, P.-F., Van Damme, M., Clerbaux, C., and Génarmont, S.: Do alternative inventories converge on the spatiotemporal representation of spring ammonia emissions in France?, *Atmos. Chem. Phys.*, 20, 13481–13495, <https://doi.org/10.5194/acp-20-13481-2020>, 2020.
- Ge, Y., Vieno, M., Stevenson, D. S., Wind, P., and Heal, M. R.: A new assessment of global and regional budgets, fluxes, and lifetimes of atmospheric reactive N and S gases and aerosols, *Atmos. Chem. Phys.*, 22, 8343–8368, <https://doi.org/10.5194/acp-22-8343-2022>, 2022.
- Grandpeix, J. Y. and Lafore, J. P.: A Density Current Parameterization Coupled with Emanuel's Convection Scheme. Part I: The Models, *J. Atmos. Sci.*, 67, 881–897, <https://doi.org/10.1175/2009JAS3044.1>, 2010.
- Granier, C., Darras, S., Denier van der Gon, H., Doubalova, J., Elguindi, N., Galle, B., Gauss, M., Guevara, M., Jalkanen, J.-P., Kuenen, J., Liousse, C., Quack, B., Simpson, D., and Sindelarova, K.: The Copernicus Atmosphere Monitoring Service global and regional emissions (April 2019 version), Copernicus Atmosphere Monitoring Service (CAMS) report, <https://doi.org/10.24380/d0bn-kx16>, 2019.
- Guo, X., Wang, R., Pan, D., Zondlo, M. A., Clarisse, L., Van Damme, M., Whitburn, S., Coheur, P. F., Clerbaux, C., Franco, B., Golston, L. M., Wendt, L., Sun, K., Tao, L., Miller, D., Mikoviny, T., Müller, M., Wisthaler, A., Tevlin, A. G., Murphy, J. G., Nowak, J. B., Roscioli, J. R., Volkamer, R., Kille, N., Neuman, J. A., Eilerman, S. J., Crawford, J. H., Yacovitch, T. I., Barrick, J. D., and Scarino, A. J.: Validation of IASI Satellite Ammonia Observations at the Pixel Scale Using In Situ Vertical Profiles, *J. Geophys. Res.-Atmos.*, 126, e2020JD033475, <https://doi.org/10.1029/2020JD033475>, 2021.
- Hauglustaine, D. A., Hourdin, F., Jourdain, L., Filiberti, M. A., Walters, S., Lamarque, J. F., and Holland, E. A.: Interactive chemistry in the Laboratoire de Météorologie Dynamique general circulation model: Description and background tropospheric chemistry evaluation, *J. Geophys. Res.-Atmos.*, 109, D04314, <https://doi.org/10.1029/2003JD003957>, 2004.
- Hauglustaine, D. A., Balkanski, Y., and Schulz, M.: A global model simulation of present and future nitrate aerosols and their direct radiative forcing of climate, *Atmos. Chem. Phys.*, 14, 11031–11063, <https://doi.org/10.5194/acp-14-11031-2014>, 2014.
- Hourdin, F., Rio, C., Grandpeix, J. Y., Madeleine, J. B., Cheruy, F., Rochetin, N., Jam, A., Musat, I., Idelkadi, A., Fairhead, L., Foujols, M. A., Mellul, L., Traore, A. K., Dufresne, J. L., Boucher, O., Lefebvre, M. P., Millour, E., Vignon, E., Jouhaud, J., Diallo, F. B., Lott, F., Gastineau, G., Caubel, A., Meurdesoif, Y., and Ghattas, J.: LMDZ6A: The Atmospheric Component of the IPSL Climate Model With Improved and Better Tuned Physics, *J. Adv. Model. Earth Sys.*, 12, e2019MS001892, <https://doi.org/10.1029/2019MS001892>, 2020.
- IASI: NH<sub>3</sub> total column from IASI (Level 2), IASI [data set], <https://iasi.aeris-data.fr/nh3/>, 2025.
- Iturbide, M., Gutiérrez, J. M., Alves, L. M., Bedia, J., Cerezo-Mota, R., Gimadevilla, E., Cofiño, A. S., Di Luca, A., Faria, S. H., Gorodetskaya, I. V., Hauser, M., Herrera, S., Hennessy, K., Hewitt, H. T., Jones, R. G., Krakovska, S., Manzanar, R., Martínez-Castro, D., Narisma, G. T., Nurhati, I. S., Pinto, I., Seneviratne, S. I., van den Hurk, B., and Vera, C. S.: An update of IPCC climate reference regions for subcontinental analysis of climate model data: definition and aggregated datasets, *Earth Syst. Sci. Data*, 12, 2959–2970, <https://doi.org/10.5194/essd-12-2959-2020>, 2020.
- Jin, J., Fang, L., Li, B., Liao, H., Wang, Y., Han, W., Li, K., Pang, M., Wu, X., and Xiang Lin, H.: 4DVar-based inversion system for ammonia emission estimation in China through assimilating IASI ammonia retrievals, *Environ. Res. Lett.*, 18, 034005, <https://doi.org/10.1088/1748-9326/ACB835>, 2023.
- Koukoulis, M. E., Theys, N., Ding, J., Zylichidou, I., Mijling, B., Balis, D., and van der A, R. J.: Updated SO<sub>2</sub> emission estimates over China using OMI/Aura observations, *Atmos. Meas. Tech.*, 11, 1817–1832, <https://doi.org/10.5194/amt-11-1817-2018>, 2018.
- Krinner, G., Viovy, N., de Noblet-Ducoudré, N., Ogée, J., Polcher, J., Friedlingstein, P., Ciais, P., Sitch, S., and Prentice, I. C.: A dynamic global vegetation model for studies of the coupled atmosphere-biosphere system, *Global Biogeochem. Cycles*, 19, 1–33, <https://doi.org/10.1029/2003GB002199>, 2005.
- Kuttippurath, J., Singh, A., Dash, S. P., Mallick, N., Clerbaux, C., Van Damme, M., Clarisse, L., Coheur, P. F., Raj, S., Abhishek, K., and Varikoden, H.: Record high levels of atmospheric ammonia over India: Spatial and temporal analyses, *Sci. Total Environ.*, 740, 139986, <https://doi.org/10.1016/J.SCITOTENV.2020.139986>, 2020.
- Kuttippurath, J., Patel, V. K., Kashyap, R., Singh, A., and Clerbaux, C.: Anomalous increase in global atmospheric ammonia during COVID-19 lockdown: Need policies to curb agricultural emissions, *J. Clean. Prod.*, 434, 140424, <https://doi.org/10.1016/J.JCLEPRO.2023.140424>, 2024.
- Lamsal, L. N., Martin, R. V., Padmanabhan, A., Van Donkelaar, A., Zhang, Q., Sioris, C. E., Chance, K., Kurosu, T. P., and Newchurch, M. J.: Application of satellite observations for timely updates to global anthropogenic NO<sub>x</sub> emission inventories, *Geophys. Res. Lett.*, 38, L05810, <https://doi.org/10.1029/2010GL046476>, 2011.

- Li, C., Martin, R. V., Shephard, M. W., Cady-Pereira, K., Cooper, M. J., Kaiser, J., Lee, C. J., Zhang, L., and Henze, D. K.: Assessing the Iterative Finite Difference Mass Balance and 4D-Var Methods to Derive Ammonia Emissions Over North America Using Synthetic Observations, *J. Geophys. Res.-Atmos.*, 124, 4222–4236, <https://doi.org/10.1029/2018JD030183>, 2019.
- Liu, P., Ding, J., Liu, L., Xu, W., and Liu, X.: Estimation of surface ammonia concentrations and emissions in China from the polar-orbiting Infrared Atmospheric Sounding Interferometer and the FY-4A Geostationary Interferometric Infrared Sounder, *Atmos. Chem. Phys.*, 22, 9099–9110, <https://doi.org/10.5194/acp-22-9099-2022>, 2022.
- Lovarelli, D., Fugazza, D., Costantini, M., Conti, C., Diolaiuti, G., and Guarino, M.: Comparison of ammonia air concentration before and during the spread of COVID-19 in Lombardy (Italy) using ground-based and satellite data, *Atmos. Environ.*, 259, 118534, <https://doi.org/10.1016/J.ATMOSENV.2021.118534>, 2021.
- Luo, Z., Zhang, Y., Chen, W., Van Damme, M., Coheur, P.-F., and Clarisse, L.: Estimating global ammonia (NH<sub>3</sub>) emissions based on IASI observations from 2008 to 2018, *Atmos. Chem. Phys.*, 22, 10375–10388, <https://doi.org/10.5194/acp-22-10375-2022>, 2022.
- Makkaron, P., Tong, D. Q., Li, Y., Hyer, E. J., Xian, P., Kondragunta, S., Campbell, P. C., Tang, Y., Baker, B. D., Cohen, M. D., Darnenov, A., Lyapustin, A., Saylor, R. D., Wang, Y., and Stajner, I.: Development and Evaluation of a North America Ensemble Wildfire Air Quality Forecast: Initial Application to the 2020 Western United States “Gigafire,” *J. Geophys. Res.-Atmos.*, 128, e2022JD037298, <https://doi.org/10.1029/2022JD037298>, 2023.
- Marais, E. A., Pandey, A. K., Van Damme, M., Clarisse, L., Coheur, P. F., Shephard, M. W., Cady-Pereira, K. E., Misselbrook, T., Zhu, L., Luo, G., and Yu, F.: UK Ammonia Emissions Estimated With Satellite Observations and GEOS-Chem, *J. Geophys. Res.-Atmos.*, 126, e2021JD035237, <https://doi.org/10.1029/2021JD035237>, 2021.
- McDuffie, E. E., Smith, S. J., O’Rourke, P., Tibrewal, K., Venkataraman, C., Marais, E. A., Zheng, B., Crippa, M., Brauer, M., and Martin, R. V.: A global anthropogenic emission inventory of atmospheric pollutants from sector- and fuel-specific sources (1970–2017): an application of the Community Emissions Data System (CEDS), *Earth Syst. Sci. Data*, 12, 3413–3442, <https://doi.org/10.5194/essd-12-3413-2020>, 2020.
- Messina, P., Lathière, J., Sindelarova, K., Vuichard, N., Granier, C., Ghattas, J., Cozic, A., and Hauglustaine, D. A.: Global biogenic volatile organic compound emissions in the ORCHIDEE and MEGAN models and sensitivity to key parameters, *Atmos. Chem. Phys.*, 16, 14169–14202, <https://doi.org/10.5194/acp-16-14169-2016>, 2016.
- Momeni, M., Choi, Y., Yeganeh, A. K., Pouyaei, A., Jung, J., Park, J., Shephard, M. W., Dammers, E., and Cady-Pereira, K. E.: Constraining East Asia Ammonia Emissions Through Satellite Observations and Iterative Finite Difference Mass Balance (iFDMB) and Investigating its Impact on Inorganic Fine Particulate Matter, *Environment International*, 184, 108473, ISSN 0160-4120, <https://doi.org/10.1016/j.envint.2024.108473>, 2024.
- Osipov, S., Chowdhury, S., Crowley, J. N., Tadic, I., Drewnick, F., Borrmann, S., Eger, P., Fachinger, F., Fischer, H., Predybaylo, E., Fnais, M., Harder, H., Pikridas, M., Vouterakos, P., Pozzer, A., Sciare, J., Ukhov, A., Stenchikov, G. L., Williams, J., and Lelieveld, J.: Severe atmospheric pollution in the Middle East is attributable to anthropogenic sources, *Commun. Earth Environ.*, 3, 1–10, <https://doi.org/10.1038/s43247-022-00514-6>, 2022.
- Pu, W., Guo, H., Ma, Z., Qiu, Y., Tang, Y., Liu, Q., Wang, F., and Sheng, J.: Aircraft measurements reveal vertical distribution of atmospheric ammonia over the North China Plain in early autumn, *Environ. Chem. Lett.*, 18, 2149–2156, <https://doi.org/10.1007/s10311-020-01051-4>, 2020.
- Rio, C. and Hourdin, F.: A Thermal Plume Model for the Convective Boundary Layer: Representation of Cumulus Clouds, *J. Atmos. Sci.*, 65, 407–425, <https://doi.org/10.1175/2007JAS2256.1>, 2008.
- Sahoo, P., Sahu, S. K., Mangaraj, P., Mishra, A., Beig, G., and Gunthe, S. S.: Reporting of gridded ammonia emission and assessment of hotspots across India: A comprehensive study of 24 anthropogenic sources, *J. Hazard. Mater.*, 479, 135557, <https://doi.org/10.1016/J.JHAZMAT.2024.135557>, 2024.
- Shephard, M. W., Dammers, E., Cady-Pereira, K. E., Kharol, S. K., Thompson, J., Gainariu-Matz, Y., Zhang, J., McLinden, C. A., Kovachik, A., Moran, M., Bittman, S., Sioris, C. E., Griffin, D., Alvarado, M. J., Lonsdale, C., Savic-Jovicic, V., and Zheng, Q.: Ammonia measurements from space with the Cross-track Infrared Sounder: characteristics and applications, *Atmos. Chem. Phys.*, 20, 2277–2302, <https://doi.org/10.5194/acp-20-2277-2020>, 2020.
- Someya, Y., Imasu, R., Shiomi, K., and Saitoh, N.: Atmospheric ammonia retrieval from the TANSO-FTS/GOSAT thermal infrared sounder, *Atmos. Meas. Tech.*, 13, 309–321, <https://doi.org/10.5194/amt-13-309-2020>, 2020.
- Soulie, A., Granier, C., Darras, S., Zilbermann, N., Doumbia, T., Guevara, M., Jalkanen, J.-P., Keita, S., Liousse, C., Crippa, M., Guizzardi, D., Hoesly, R., and Smith, S. J.: Global Anthropogenic Emissions (CAMSGLOB-ANT) for the Copernicus Atmosphere Monitoring Service Simulations of Air Quality Forecasts and Reanalyses, ECCAD [data set], <https://doi.org/10.24380/eets-qd81>, 2023.
- Soulie, A., Granier, C., Darras, S., Zilbermann, N., Doumbia, T., Guevara, M., Jalkanen, J.-P., Keita, S., Liousse, C., Crippa, M., Guizzardi, D., Hoesly, R., and Smith, S. J.: Global anthropogenic emissions (CAMSGLOB-ANT) for the Copernicus Atmosphere Monitoring Service simulations of air quality forecasts and reanalyses, *Earth Syst. Sci. Data*, 16, 2261–2279, <https://doi.org/10.5194/essd-16-2261-2024>, 2024.
- Sutton, M. A., Reis, S., Riddick, S. N., Dragosits, U., Nemitz, E., Theobald, M. R., Tang, Y. S., Braban, C. F., Viena, M., Dore, A. J., Mitchell, R. F., Wanless, S., Daunt, F., Fowler, D., Blackall, T. D., Milford, C., Flechard, C. R., Loubet, B., Massad, R., Cellier, P., Personne, E., Coheur, P. F., Clarisse, L., Van Damme, M., Ngadi, Y., Clerbaux, C., Skj  th, C. A., Geels, C., Hertel, O., Kruit, R. J. W., Pinder, R. W., Bash, J. O., Walker, J. T., Simpson, D., Horv  th, L., Misselbrook, T. H., Bleeker, A., Dentener, F., and de Vries, W.: Towards a climate-dependent paradigm of ammonia emission and deposition, *Philos. T. Roy. Soc. B*, 368, 20130166, <https://doi.org/10.1098/RSTB.2013.0166>, 2013.
- Tich  y, O., Eckhardt, S., Balkanski, Y., Hauglustaine, D., and Evangelou, N.: Decreasing trends of ammonia emissions over Europe seen from remote sensing and inverse modelling, *Atmos. Chem.*



- Phys., 23, 15235–15252, <https://doi.org/10.5194/acp-23-15235-2023>, 2023.
- Van Damme, M., Clarisse, L., Heald, C. L., Hurtmans, D., Ngadi, Y., Clerbaux, C., Dolman, A. J., Erismann, J. W., and Coheur, P. F.: Global distributions, time series and error characterization of atmospheric ammonia (NH<sub>3</sub>) from IASI satellite observations, *Atmos. Chem. Phys.*, 14, 2905–2922, <https://doi.org/10.5194/acp-14-2905-2014>, 2014.
- Van Damme, M., Whitburn, S., Clarisse, L., Clerbaux, C., Hurtmans, D., and Coheur, P.-F.: Version 2 of the IASI NH<sub>3</sub> neural network retrieval algorithm: near-real-time and reanalysed datasets, *Atmos. Meas. Tech.*, 10, 4905–4914, <https://doi.org/10.5194/amt-10-4905-2017>, 2017.
- Van Damme, M., Clarisse, L., Whitburn, S., Hadji-Lazaro, J., Hurtmans, D., Clerbaux, C., and Coheur, P. F.: Industrial and agricultural ammonia point sources exposed, *Nature*, 564, 99–103, <https://doi.org/10.1038/s41586-018-0747-1>, 2018.
- Van Damme, M., Clarisse, L., Franco, B., Sutton, M. A., Erismann, J. W., Wichink Kruit, R., Van Zanten, M., Whitburn, S., Hadji-Lazaro, J., Hurtmans, D., Clerbaux, C., and Coheur, P. F.: Global, regional and national trends of atmospheric ammonia derived from a decadal (2008–2018) satellite record, *Environ. Res. Lett.*, 16, 055017, <https://doi.org/10.1088/1748-9326/ABD5E0>, 2021.
- van der Graaf, S., Dammers, E., Segers, A., Kranenburg, R., Schaap, M., Shephard, M. W., and Erismann, J. W.: Data assimilation of CrIS NH<sub>3</sub> satellite observations for improving spatiotemporal NH<sub>3</sub> distributions in LOTOS-EUROS, *Atmos. Chem. Phys.*, 22, 951–972, <https://doi.org/10.5194/acp-22-951-2022>, 2022.
- van der Werf, G. R., Randerson, J. T., Giglio, L., van Leeuwen, T. T., Chen, Y., Rogers, B. M., Mu, M., van Marle, M. J. E., Morton, D. C., Collatz, G. J., Yokelson, R. J., and Kasibhatla, P. S.: Global fire emissions estimates during 1997–2016, *Earth Syst. Sci. Data*, 9, 697–720, <https://doi.org/10.5194/essd-9-697-2017>, 2017.
- Viatte, C., Petit, J. E., Yamanouchi, S., Van Damme, M., Doucerain, C., Germain-Piaulenne, E., Gros, V., Favez, O., Clarisse, L., Coheur, P. F., Strong, K., and Clerbaux, C.: Ammonia and PM<sub>2.5</sub> Air Pollution in Paris during the 2020 COVID Lockdown, *Atmosphere*, 12, 160, <https://doi.org/10.3390/ATMOS12020160>, 2021.
- Vira, J., Hess, P., Melkonian, J., and Wieder, W. R.: An improved mechanistic model for ammonia volatilization in Earth system models: Flow of Agricultural Nitrogen version 2 (FANv2), *Geosci. Model Dev.*, 13, 4459–4490, <https://doi.org/10.5194/gmd-13-4459-2020>, 2020.
- Wang, W., Liu, C., Clarisse, L., Van Damme, M., Coheur, P.-F., Xie, Y., Shan, C., Hu, Q., Zhang, H., Sun, Y., Yin, H., and Jones, N.: Spatial distribution and seasonal variability in atmospheric ammonia measured from ground-based FTIR observations at Hefei, China, *Atmos. Meas. Tech. Discuss.* [preprint], <https://doi.org/10.5194/amt-2020-39>, 2020.
- Warner, J. X., Wei, Z., Strow, L. L., Dickerson, R. R., and Nowak, J. B.: The global tropospheric ammonia distribution as seen in the 13-year AIRS measurement record, *Atmos. Chem. Phys.*, 16, 5467–5479, <https://doi.org/10.5194/acp-16-5467-2016>, 2016.
- Whitburn, S., Van Damme, M., Clarisse, L., Bauduin, S., Heald, C. L., Hadji-Lazaro, J., Hurtmans, D., Zondlo, M. A., Clerbaux, C., and Coheur, P. F.: A flexible and robust neural network IASI-NH<sub>3</sub> retrieval algorithm, *J. Geophys. Res.-Atmos.*, 121, 6581–6599, <https://doi.org/10.1002/2016JD024828>, 2016.
- Wyer, K. E., Kelleghan, D. B., Blanes-Vidal, V., Schaubberger, G., and Curran, T. P.: Ammonia emissions from agriculture and their contribution to fine particulate matter: A review of implications for human health, *J. Environ. Manage.*, 323, 116285, <https://doi.org/10.1016/J.JENVMAN.2022.116285>, 2022.
- Xia, J., Zhou, Y., Fang, L., Qi, Y., Li, D., Liao, H., and Jin, J.: South Asia anthropogenic ammonia emission inversion through assimilating IASI observations, *Atmos. Chem. Phys.*, 25, 7071–7086, <https://doi.org/10.5194/acp-25-7071-2025>, 2025.
- Xu, R., Tian, H., Pan, S., Prior, S. A., Feng, Y., Batchelor, W. D., Chen, J., and Yang, J.: Global ammonia emissions from synthetic nitrogen fertilizer applications in agricultural systems: Empirical and process-based estimates and uncertainty, *Glob. Chang. Biol.*, 25, 314–326, <https://doi.org/10.1111/GCB.14499>, 2019.
- Xu, R. T., Pan, S. F., Chen, J., Chen, G. S., Yang, J., Dangal, S. R. S., Shepard, J. P., and Tian, H. Q.: Half-Century Ammonia Emissions From Agricultural Systems in Southern Asia: Magnitude, Spatiotemporal Patterns, and Implications for Human Health, *Geohealth*, 2, 40–53, <https://doi.org/10.1002/2017GH000098>, 2018.
- Xu, W., Zhao, Y., Wen, Z., Chang, Y., Pan, Y., Sun, Y., Ma, X., Sha, Z., Li, Z., Kang, J., Liu, L., Tang, A., Wang, K., Zhang, Y., Guo, Y., Zhang, L., Sheng, L., Zhang, X., Gu, B., Song, Y., Van Damme, M., Clarisse, L., Coheur, P. F., Collett, J. L., Goulding, K., Zhang, F., He, K., and Liu, X.: Increasing importance of ammonia emission abatement in PM<sub>2.5</sub> pollution control, *Sci. Bull. (Beijing)*, 67, 1745–1749, <https://doi.org/10.1016/J.SCIB.2022.07.021>, 2022.
- Yamada, T.: Simulations of Nocturnal Drainage Flows by a  $q^2l$  Turbulence Closure Model, *J. Atmos. Sci.*, 40, 91–106, [https://doi.org/10.1175/1520-0469\(1983\)040<0091:SONDFB>2.0.CO;2](https://doi.org/10.1175/1520-0469(1983)040<0091:SONDFB>2.0.CO;2), 1983.
- Zheng, B., Geng, G., Ciais, P., Davis, S. J., Martin, R. V., Meng, J., Wu, N., Chevallier, F., Broquet, G., Boersma, F., van Der, R. A., Lin, J., Guan, D., Lei, Y., He, K., and Zhang, Q.: Satellite-based estimates of decline and rebound in China's CO<sub>2</sub> emissions during COVID-19 pandemic, *Sci. Adv.*, 6, <https://doi.org/10.1126/sciadv.abd4998>, 2020.
- Zheng, B., Zhang, Q., Geng, G., Chen, C., Shi, Q., Cui, M., Lei, Y., and He, K.: Changes in China's anthropogenic emissions and air quality during the COVID-19 pandemic in 2020, *Earth Syst. Sci. Data*, 13, 2895–2907, <https://doi.org/10.5194/essd-13-2895-2021>, 2021.
- Zhu, L., Henze, D. K., Bash, J. O., Cady-Pereira, K. E., Shephard, M. W., Luo, M., and Capps, S. L.: Sources and Impacts of Atmospheric NH<sub>3</sub>: Current Understanding and Frontiers for Modeling, Measurements, and Remote Sensing in North America, *Curr. Pollut. Rep.*, 1, 95–116, <https://doi.org/10.1007/s40726-015-0010-4>, 2015.